

On the equivalence between the cell-based smoothed finite element method and the virtual element method

Sundararajan Natarajan^{a*}, Stéphane PA Bordas^b, Ean Tat Ooi^c

^a*School of Civil and Environmental Engineering, The University of New South Wales, Sydney, NSW 2052, Australia.*

^b*Faculté des Sciences, de la Technologie et de la Communication, University of Luxembourg, Luxembourg.*

^c*School of Science, Information Technology and Engineering, Federation University, Ballarat, VIC 3353, Australia.*

SUMMARY

We revisit the cell-based smoothed finite element method (SFEM) for quadrilateral elements and extend it to arbitrary polygons and polyhedrons in 2D and 3D, respectively. We highlight the similarity between the SFEM and the virtual element method (VEM). Based on the VEM, we propose a new stabilization approach to the SFEM when applied to arbitrary polygons and polyhedrons. The accuracy and the convergence properties of the SFEM are studied with a few benchmark problems in 2D and 3D linear elasticity. Later, the SFEM is combined with the scaled boundary finite element method to problems involving singularity within the framework of the linear elastic fracture mechanics in 2D. Copyright © 2013 John Wiley & Sons, Ltd.

Received . . .

KEY WORDS: smoothed finite element method, virtual element method, boundary integration, scaled boundary finite element method, polyhedron.

1. INTRODUCTION

The finite element method (FEM) relies on discretizing the domain with non-overlapping regions, called the ‘elements’. In the conventional FEM, the topology of the elements were restricted to triangles and quadrilaterals in 2D or tetrahedrals and hexahedrals in 3D. The use of such standard shapes, simplifies the approach, however, this may require sophisticated (re-) meshing algorithms to either generate high-quality meshes or to capture the topological changes. Moreover, the accuracy of the solution depends on the quality of the element employed. Lee and Bathe [1] observed that the shape functions lose their ability to reproduce the displacement fields when the mesh is distorted. In an effort to overcome the limitations of the FEM, the research has been focussed on:

- De-coupling geometry and analysis, for example, meshfree methods [2, 3], PU enrichment [4, 5], Immersed boundary method [6].
- Improve the element formulations
 - Strain smoothing [7]
 - Unsymmetric formulation [8, 9]
 - hybrid Trefftz FEM [10, 11]
 - Polygonal FEM [12]
- Coupling geometry and analysis, for example, isogeometric analysis [13, 14].
- Boundary based methods, for example, boundary element method [15], scaled boundary finite element method [16].

*Correspondence to: School of Civil and Environmental Engineering, The University of New South Wales, Sydney, NSW 2052, Australia. Email: snatarajan@cardiffalumni.org.uk. Tel: +61 9358 5030.

In this study, we focus on the work on the improvement of the finite element formulation, in particular, the strain smoothing technique [17] and the polygonal finite element method [18].

1.1. Background

Liu *et al.*, [17], extended the concept of stabilized conforming nodal integration (SCNI) [19] to finite element approximations and coined the resulting method the Smoothed Finite Element Method (SFEM). Liu *et al.* formulated a series of SFEM models name as cell-based SFEM (CSFEM) [7], node based SFEM (NSFEM) [20], edge-based SFEM (ESFEM) [21], face-based SFEM (FSFEM) [22] and alpha-FEM [23]. All these SFEM models use finite element mesh with linear interpolants. In the SFEM, in particular, CSFEM, the elements are divided into smoothing cells, over which the standard (compatible) strain field is smoothed. This smoothing allows to transform the volume integration into surface integration by employing the divergence theorem and hence the computation of the stiffness matrix requires only the information on the boundary of the subcells. It should be noted that only the CSFEM employs quadrilateral elements, whilst all other SFEM models employ triangular elements as the background mesh. When the CSFEM is employed to triangular elements, the resulting stiffness matrix is similar to the conventional FEM. The convergence, stability, accuracy and computational complexity of this method were studied in detail in [24]. The method was further extended to treat various problems in solid mechanics such as plates [25], shells [26], nearly incompressible elasticity [27, 28], to name a few. Recently, the strain smoothing method was combined with enrichment methods in [29, 30] to model problems with strong discontinuity and singularities. However, certain difficulties still exist as discussed in [29].

On another related front, polygonal finite element methods (PFEM) has been receiving increasing attention in recent years. In PFEM, the domain can be discretized without a need to maintain a particular element topology (see Figure (1)). Moreover, this is advantageous in adaptive mesh refinement, where a straightforward subdivision of individual elements usually results in hanging nodes (see Figure (1)). Conventionally, this is eliminated by introducing additional edges/faces to retain conformity. This can be avoided if we can compute directly on polyhedral meshes with hanging nodes.

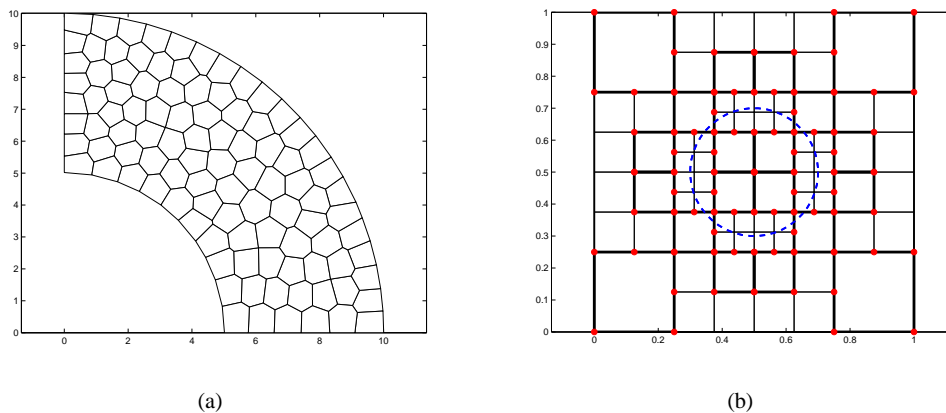


Figure 1. Domain discretized with finite elements: (a) discretization with arbitrary polygons and (b) adaptive refinement leading to a quadtree mesh, where the ‘dotted’ line represents an inner boundary and the ‘highlighted’ elements are the elements with hanging nodes.

In 1971, Wachspress [31] developed a method based on rational basis functions for generalizations to elements with arbitrary number of sides. However, these elements were not used because of the associated difficulties, such as in constructing the basis functions and the numerical integration of the basis functions. Thanks to advancement in mathematical softwares, viz., Mathematica[®] and Maple[®] and the pioneering work of Alwood and Cornes [15], Sukumar and Tabarraei [16], Dasgupta [17], to name a few, now discretization of the domain with finite

elements having arbitrary number of sides is plausible. Once the basis functions are constructed, the conventional Galerkin procedure is normally employed to solve the governing equations over the polygonal/polyhedral meshes. However, the difficulty with these techniques is associated to the numerical integration of the terms in the stiffness matrix over polygonal/polyhedral meshes. Improving numerical integration over polytopes has gained increasing attention in the recent literature [32, 33, 34, 35, 36]. Dai *et al.*, [37] employed the strain smoothing technique over arbitrary polygons. It was observed that, the arbitrary polygons must have a minimum of n subcells (where n is the number of sides of the polygon > 4) to ensure stability. Recently, Natarajan *et al.*, [38] and Ooi *et al.*, [39] employed the scaled boundary finite element method over arbitrary polygons for linear elasticity and linear elastic fracture mechanics, respectively.

Recently, the concept of virtual element method (VEM) has received increasing attention among researchers [40, 41, 42, 18]. The VEM has evolved from the mimetic difference methods [40]. The VEM is a Galerkin approach, however, unlike the conventional FEM, the VEM does not require an explicit form of the basis functions to compute the stiffness matrix. Moreover, the VEM can be employed over arbitrary polygons and polyhedrons. Within the framework of the VEM, the space within an element of decomposition[†], contains a certain polynomials that guarantee *accuracy* and additional functions for stability. The VEM alleviates the numerical integration difficulty encountered in the conventional polygonal FEM. As the method does not require the knowledge of the explicit form of the shape functions, the implementation is computationally less intensive.

1.2. Objective

The strain smoothing technique can be applied to arbitrary polygons. However, it was observed in [38] that the strain smoothing technique over arbitrary polytopes yielded less accurate solution when compared to other techniques, such as the conventional polygonal finite element method. The main objective of this paper is:

- to revisit the strain smoothing technique, in particular, the cell based SFEM and extend to arbitrary polygons and polyhedrons.
- investigate the equivalence between the strain smoothing technique and the VEM.
- propose a new stabilization for the SFEM with one subcell based on the concept of the VEM.
- to study the accuracy and the convergence properties of the SFEM with new stabilization technique.
- to couple the SFEM with the scaled boundary finite element method (SBFEM) (see Section 5.3 for a detailed discussion on the SBFEM) to study problems with strong discontinuity and singularities.

Through out this paper, SFEM represents the cell-based smoothed finite element method unless mentioned otherwise.

1.3. Outline

The paper is organized as follows. Section 2 recalls the basics of the cell-based smoothed finite element method as applied to 2D and 3D elasticity. Section 3 briefly reviews the virtual element method. The similarity between the SFEM and the VEM is discussed in Section 4. Some numerical examples are analyzed to demonstrate the accuracy and the convergence properties of the cell-based smoothed finite element method in Section 5 with a few problems taken from linear elasticity. The SFEM is combined with the SBFEM and the accuracy of the approach is demonstrated with a few benchmark problems in linear elastic fracture mechanics. Conclusions and future work are presented in the final section.

[†]There is no restriction on the shape of the element in VEM

2. OVERVIEW OF THE SMOOTHED FINITE ELEMENT METHOD

2.1. Background

The strain-smoothing method (SSM) was proposed in [19] where the strain is written as the divergence of a spatial average of the standard (compatible) strain field –i.e. symmetric gradient of the displacement field. In the cell-based SFEM, the elements are divided into subcells as shown in Figure (2). The strain field $\tilde{\varepsilon}_{ij}^h$, used to compute the stiffness matrix is computed by a weighted average of the standard strain field ε_{ij}^h . At a point \mathbf{x}_C in an element Ω^h ,

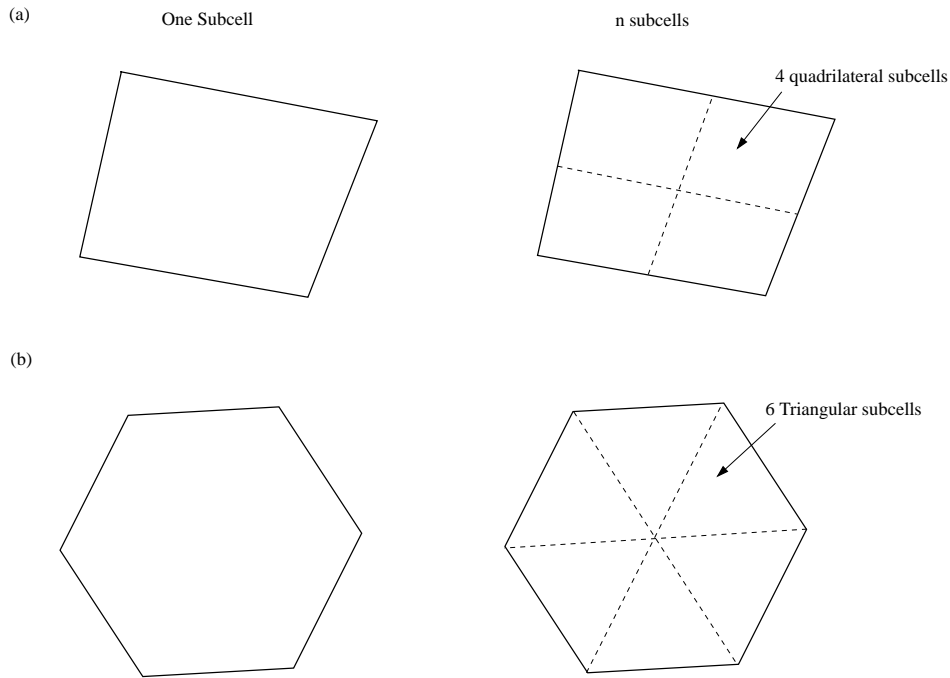


Figure 2. Subdivision of an element into subcells: (a) quadrilateral element and (b) arbitrary polygon.

$$\tilde{\varepsilon}_{ij}^h(\mathbf{x}_C) = \int_{\Omega^h} \varepsilon_{ij}^h(\mathbf{x}) \Phi(\mathbf{x} - \mathbf{x}_C) d\mathbf{x} \quad (1)$$

where Φ is a smoothing function that generally satisfies the following properties [43]

$$\Phi \geq 0 \quad \text{and} \quad \int_{\Omega^h} \Phi(\mathbf{x}) d\mathbf{x} = 1 \quad (2)$$

$$\Phi = \frac{1}{A_C} \quad \text{in} \quad \Omega_C \quad \text{and} \quad \Phi = 0 \quad \text{elsewhere} \quad (3)$$

To use Equation (1), the subcell containing point \mathbf{x}_C must first be located in order to compute the correct value of the weight function Φ . The discretised strain field is computed, through the so-called smoothed discretised gradient operator $\tilde{\mathbf{B}}$, defined by (see Figure (3) for a schematic representation of the construction)

$$\tilde{\varepsilon}^h(\mathbf{x}_C) = \tilde{\mathbf{B}}_C(\mathbf{x}_C) \mathbf{q} \quad (4)$$

where the \mathbf{q} are unknown displacements coefficients defined at the node of the finite element, as usual. The smoothed element stiffness matrix for element e is computed by the *sum of the*

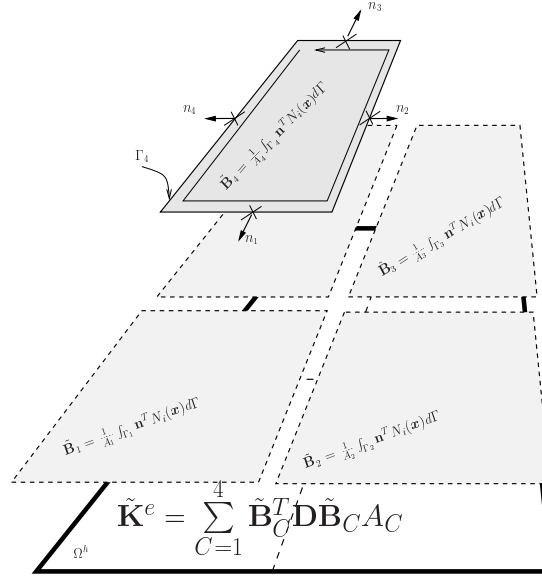


Figure 3. Calculation of the smoothed discretized gradient operator.

contributions of the subcells (Figure (3))[‡]

$$\tilde{\mathbf{K}}^e = \sum_{C=1}^{nc} \int_{\Omega_C} \tilde{\mathbf{B}}_C^T \mathbf{D} \tilde{\mathbf{B}}_C d\Omega = \sum_{C=1}^{nc} \tilde{\mathbf{B}}_C^T \mathbf{D} \tilde{\mathbf{B}}_C \int_{\Omega_C} d\Omega = \sum_{C=1}^{nc} \tilde{\mathbf{B}}_C^T \mathbf{D} \tilde{\mathbf{B}}_C A_C \quad (5)$$

where nc is the number of the smoothing cells of the element. The strain displacement matrix $\tilde{\mathbf{B}}_C$ is constant over each Ω_C and is of the following form

$$\tilde{\mathbf{B}}_C = [\tilde{\mathbf{B}}_{C1} \quad \tilde{\mathbf{B}}_{C2} \quad \tilde{\mathbf{B}}_{C3} \quad \cdots \quad \tilde{\mathbf{B}}_{Cn}] \quad (6)$$

where for all shape functions $I \in \{1, \dots, n\}$, the 3×2 submatrix $\tilde{\mathbf{B}}_{CI}$ represents the contribution to the strain displacement matrix associated with shape function I and cell C and writes (see Figure (3))

$$\begin{aligned} \forall I \in \{1, 2, \dots, n\}, \forall C \in \{1, 2, \dots, nc\} \tilde{\mathbf{B}}_{CI} &= \frac{1}{A_C} \int_{S_C} \mathbf{n}^T(\mathbf{x}) N_I(\mathbf{x}) dS \\ &= \frac{1}{A_C} \int_{S_C} \begin{bmatrix} n_x & 0 \\ 0 & n_y \\ n_y & n_x \end{bmatrix} (\mathbf{x}) N_I(\mathbf{x}) dS \end{aligned} \quad (7)$$

Note that since Equation (7) is computed on the boundary of Ω_C and one Gauß point is sufficient for an exact integration:

$$\tilde{\mathbf{B}}_{CI}(\mathbf{x}_C) = \frac{1}{A_C} \sum_{b=1}^{nb} \begin{pmatrix} N_I(\mathbf{x}_b^G) n_x & 0 \\ 0 & N_I(\mathbf{x}_b^G) n_y \\ N_I(\mathbf{x}_b^G) n_y & N_I(\mathbf{x}_b^G) n_x \end{pmatrix} l_b^C \quad (8)$$

where \mathbf{x}_b^G and l_b^C are the center point (Gauß point) and the length of Γ_b^C , respectively. Until now, no assumption has been made on the shape of the element. The procedure outlined so far is general

[‡]The subcells Ω_C form a partition of the element Ω^h .

and is applicable to polygons of arbitrary shapes [37, 38]. Due to the process of strain smoothing, only the shape function is involved in the calculation of the field gradients and hence the stiffness matrix. In this study, we employ the simple averaging technique to compute the shape functions over arbitrary polygons. The construction of shape function is as follows: for a general polygonal element, a central point O is located by:

$$(x_o, y_o) = \frac{1}{n} \sum_i^n (x_i, y_i) \quad (9)$$

where n is the number of nodes of the polygonal element. The shape function at point O is given by $[1/n \cdots 1/n]$ with size $1 \times n$.

2.2. Extension to 3D

As in the 2D, the smoothed element stiffness matrix is the sum over the subcells of the contribution from each subcell[§] (see Figure (4)), which is constant:

$$\tilde{\mathbf{K}}^e = \sum_{C=1}^{nc} \int_{\Omega_C} \tilde{\mathbf{B}}_C^T \mathbf{D} \tilde{\mathbf{B}}_C d\Omega = \sum_{C=1}^{nc} \tilde{\mathbf{B}}_C^T \mathbf{D} \tilde{\mathbf{B}}_C \int_{\Omega_C} d\Omega = \sum_{C=1}^{nc} \tilde{\mathbf{B}}_C^T \mathbf{D} \tilde{\mathbf{B}}_C V_C \quad (10)$$

The strain-displacement matrix $\tilde{\mathbf{B}}_C$ is constant over each Ω_C and is of the following form:

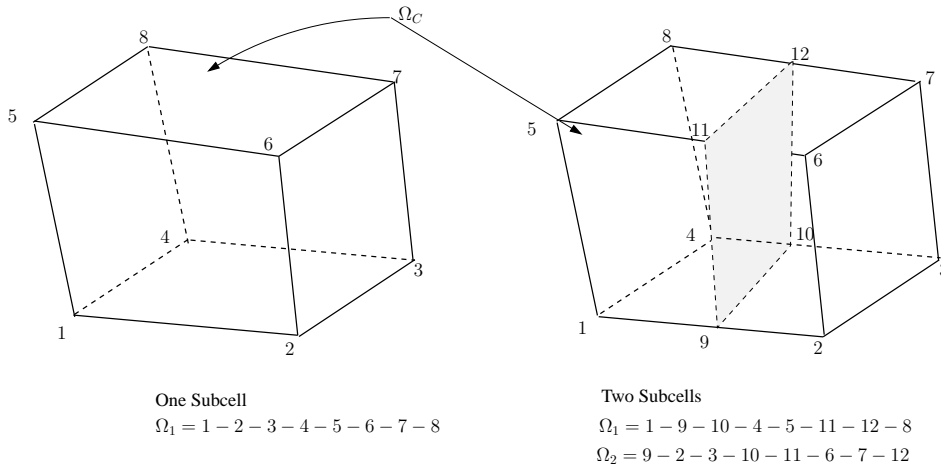


Figure 4. Subdivision of an element into subcells: (a) quadrilateral element and (b) arbitrary polygon.

$$\tilde{\mathbf{B}}_C = [\tilde{\mathbf{B}}_{C1} \quad \tilde{\mathbf{B}}_{C2} \quad \tilde{\mathbf{B}}_{C3} \quad \cdots \quad \tilde{\mathbf{B}}_{Cn}] \quad (11)$$

where for all shape functions $I \in \{1, \dots, n\}$, the 6×3 submatrix $\tilde{\mathbf{B}}_{CI}$ represents the contribution to the strain displacement matrix associated with shape function I and cell C and writes :

$$\begin{aligned} \forall I \in \{1, 2, \dots, n\}, \forall C \in \{1, 2, \dots, nc\} \tilde{\mathbf{B}}_{CI} &= \frac{1}{V_C} \int_{S_C} \mathbf{n}^T(\mathbf{x}) N_I(\mathbf{x}) dS \\ &= \frac{1}{V_C} \int_{S_C} \begin{bmatrix} n_x & 0 & 0 \\ 0 & n_y & 0 \\ 0 & 0 & n_z \\ n_y & n_x & 0 \\ 0 & n_z & n_y \\ n_z & 0 & n_x \end{bmatrix} (\mathbf{x}) N_I(\mathbf{x}) dS \quad (12) \end{aligned}$$

[§]Note that in 3D, the subcell is a volume

As in 2D, due to the process of strain smoothing, only the shape function is involved in the calculation of the field gradient and hence the stiffness matrix. In this study, over an arbitrary polygonal surface, we employ Wachspress interpolants [31]. When the strain smoothing is employed to three-dimensional domain, the volume integral is transferred to the surface integral. This surface integral is over the polygonal surfaces that build up the polyhedron. In computing the strain-displacement matrix given by Equation (12) and the stiffness matrix, only the shape functions associated with the polygonal surface contribute to the integral. To evaluate the integral in Equation (12), two schemes are adopted [44]: (a) nodal quadrature and (b) conforming interpolant quadrature.

Nodal quadrature In this case, the surface integral of the shape function N_I over any face of the polyhedral element is given by:

$$\int_{S_C} N_I(\mathbf{x}) \, dS = N_I(\mathbf{x}_I) A_I = A_I \quad (13)$$

where A_I is the nodal weight of the node I , which is the area of the quadrilateral formed by the node, the centroid of the face and the mid-points of the edges containing the node. This is depicted in Figure (5), however, this scheme is applicable only to the elements where the star convexity is satisfied.

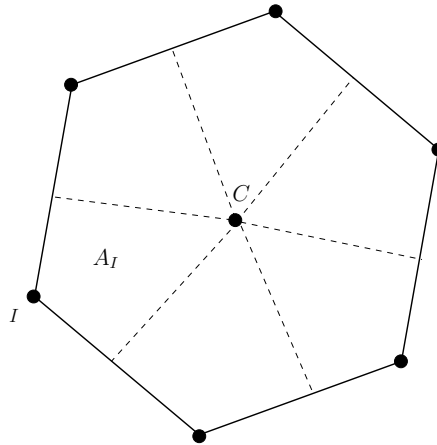


Figure 5. Nodal quadrature, where I is any node, A_I is the area formed by the node, the centroid C and the mid-points of the edges containing the node I .

Conforming Interpolant quadrature In this case, to evaluate the surface integral of the shape function N_I , we adopt interpolation scheme. For this purpose, the knowledge of the shape functions within the polygonal surface is required and in this study, we employ Wachspress interpolants [31] over the polygonal surface. To integrate the terms in the strain-displacement matrix, the polygonal surface is mapped onto a regular polygon. The regular polygon is sub-divided into triangles and triangular quadrature rules over each triangle are employed to numerically integrate the terms in Equation (12) (see Figure (6)). This process involves two level iso-parametric mapping of the surface and relies on the positivity of the Jacobian matrix involved in the transformation. The other possible approaches include: (a) complex mapping [45, 33]; (b) adaptively weighted numerical integration scheme [46]; (c) generalized Gaussian quadrature rules [34] and (d) Gauss-Green cubature [47], to name a few.

Standard triangular element

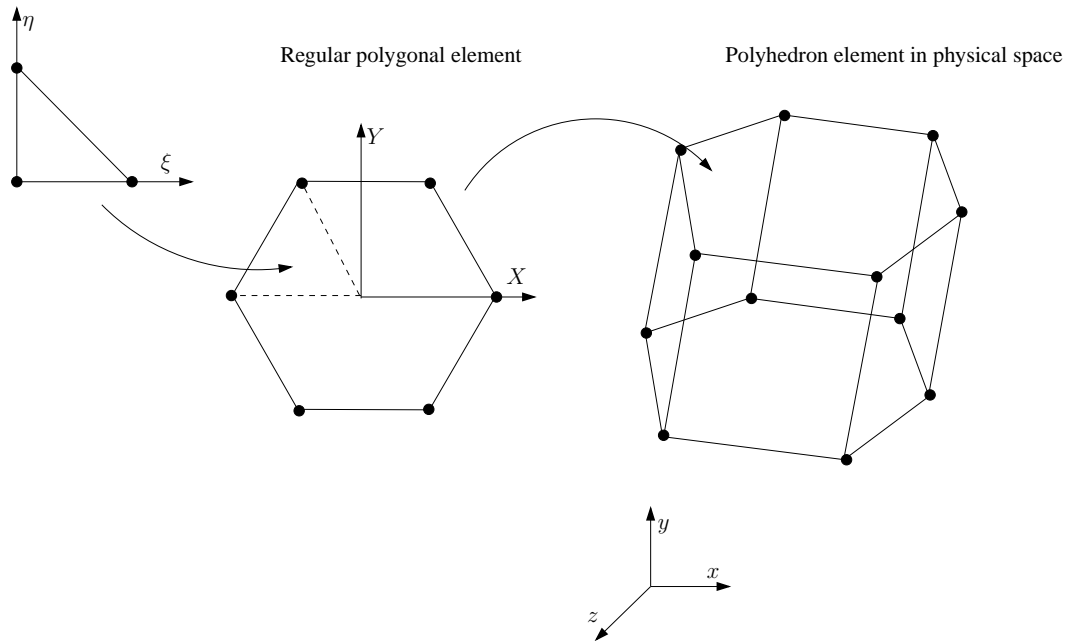


Figure 6. Surface integration scheme. The polygonal surface of a polyhedra is mapped onto a regular polygon. The regular polygon is then sub-divided into triangles and each of those sub-triangle is then mapped onto a standard triangle. Quadrature rules over the triangle are employed for the purpose of numerical integration. 'Filled' circles denote the nodes.

3. BASICS OF THE VIRTUAL ELEMENT METHOD

The virtual element method can be seen as a generalization of the finite element method to arbitrary polygons and polyhedrons. The VEM does not require the use for quadrature formulas to compute the stiffness matrix nor an expression for the basis functions. The explicit computation of the basis functions is actually not needed and this is the reason of the word 'Virtual' in the VEM [48]. The important ingredient is the operator Π^∇ that relates to the bilinear form of the problem. Once this is known, the local element stiffness matrix can be computed. It is beyond the scope of this paper to discuss the details of the VEM as applied to scalar and elasticity problems. Only important equations pertaining to the computation of the stiffness matrix associated to an arbitrary polygon/polyhedron is given in this section. Interested readers are referred to the work of Beirão Da Veiga *et al.*, [48] for scalar problems and Beirão Da Veiga *et al.*, [49] and Gain *et al.*, [44] for three dimensional elasticity, where the method is dealt with great detail. In this section, we only present the final expression to compute the stiffness matrix by the VEM pertaining to three dimensional linear elasticity. For more detailed derivation and discussion, interested readers are referred to the work of Gain *et al.*, [44]. The expression for the stiffness matrix can be written as:

$$\mathbf{K}_h^E = \underbrace{|E| \mathbf{W}_C \mathbf{D} \mathbf{W}_C^T}_{\text{Consistency term}=\mathbf{K}_{\text{const}}} + \underbrace{(\mathbf{I} - \mathbf{P}_p)^T \mathbf{S}^E (\mathbf{I} - \mathbf{P}_p)}_{\text{Stability term}=\mathbf{K}_{\text{stab}}} \quad (14)$$

where

$$\mathbf{P}_p = \mathbf{P}_R + \mathbf{P}_C \quad (15)$$

and

$$\begin{aligned} \mathbf{P}_R &= \mathbf{N}_R \mathbf{W}_R^T \\ \mathbf{P}_C &= \mathbf{N}_C \mathbf{W}_C^T \end{aligned} \quad (16)$$

where \mathbf{P}_R and \mathbf{P}_C are the projection maps of π_R and π_C , given by:

$$\begin{aligned}\pi_R &= \sum \mathbf{P}_R \mathbf{N} \\ \pi_C &= \sum \mathbf{P}_C \mathbf{N}\end{aligned}\quad (17)$$

The block $3I - 2: 3I$ rows of \mathbf{N}_R and \mathbf{N}_C are expressed as:

$$\begin{aligned}\mathbf{N}_R(3I - 2: 3) &= \begin{bmatrix} 1 & 0 & 0 & (\mathbf{x}_I - \bar{\mathbf{x}})_2 & 0 & (\mathbf{x}_I - \bar{\mathbf{x}})_3 \\ 0 & 1 & 0 & -(\mathbf{x}_I - \bar{\mathbf{x}})_1 & (\mathbf{x}_I - \bar{\mathbf{x}})_3 & 0 \\ 0 & 0 & 1 & 0 & -(\mathbf{x}_I - \bar{\mathbf{x}})_2 & (\mathbf{x}_I - \bar{\mathbf{x}})_1 \end{bmatrix} \\ \mathbf{N}_C(3I - 2: 3) &= \begin{bmatrix} (\mathbf{x}_I - \bar{\mathbf{x}})_1 & 0 & 0 & (\mathbf{x}_I - \bar{\mathbf{x}})_2 & 0 & (\mathbf{x}_I - \bar{\mathbf{x}})_3 \\ 0 & (\mathbf{x}_I - \bar{\mathbf{x}})_2 & (\mathbf{x}_I - \bar{\mathbf{x}})_1 & (\mathbf{x}_I - \bar{\mathbf{x}})_3 & 0 & 0 \\ 0 & 0 & (\mathbf{x}_I - \bar{\mathbf{x}})_3 & 0 & (\mathbf{x}_I - \bar{\mathbf{x}})_2 & (\mathbf{x}_I - \bar{\mathbf{x}})_1 \end{bmatrix}\end{aligned}\quad (18)$$

where \mathbf{x}_I is the coordinate of the ndoe and $\bar{\mathbf{x}}$ is the polyhedron centroid. The block $3I - 2: 3I$ rows of \mathbf{W}_R and \mathbf{W}_C are expressed as:

$$\begin{aligned}\mathbf{W}_R(3I - 2: 3) &= \begin{bmatrix} 1/n & 0 & 0 & (\mathbf{q}_I)_2 & 0 & -(\mathbf{q}_I)_3 \\ 0 & 1/n & 0 & -(\mathbf{q}_I)_1 & (\mathbf{q}_I)_3 & 0 \\ 0 & 0 & 1/n & 0 & -(\mathbf{q}_I)_2 & (\mathbf{q}_I)_1 \end{bmatrix} \\ \mathbf{W}_C(3I - 2: 3) &= \begin{bmatrix} 2(\mathbf{q}_I)_1 & 0 & 0 & (\mathbf{q}_I)_2 & 0 & (\mathbf{q}_I)_3 \\ 0 & 2(\mathbf{q}_I)_2 & 0 & (\mathbf{q}_I)_1 & (\mathbf{q}_I)_3 & 0 \\ 0 & 0 & 2(\mathbf{q}_I)_3 & 0 & (\mathbf{q}_I)_2 & (\mathbf{q}_I)_1 \end{bmatrix}\end{aligned}\quad (19)$$

where the subscript indicates the component of the associated vector and

$$\mathbf{q}_I = \frac{1}{2|E|} \int_{\partial E} N_I \mathbf{n} \, d\Gamma$$

where $\mathbf{S}^E = \alpha \mathbf{I}$ and $\alpha = \alpha^* \text{trace}(|E| \mathbf{W}_C \mathbf{D} \mathbf{W}_C^T)$ is a scaling coefficient. It can be seen that the computation of the stiffness matrix involves computing the matrices $\mathbf{N}_R, \mathbf{N}_C, \mathbf{W}_R$ and \mathbf{W}_C . The calculation of the matrices \mathbf{W}_R and \mathbf{W}_C involves computing the surface integral of the basis functions. This can be computed by employing one of the techniques discussed in the previous section.

4. SIMILARITY BETWEEN THE SFEM AND THE VEM

In this section, to demonstrate the similarity between the SFEM and the VEM, we compute the stiffness matrix of: (a) a quadrilateral element and (b) a pentagon. We do this for the following model problem in two dimensions:

$$\Delta u = f \text{ in } \Omega; \quad u = 0 \text{ on } \partial\Omega \quad (20)$$

where $\Omega \in \mathbb{R}^2$. The corresponding variational formulation reads: find $u \in \mathcal{V} := H_0^1(\Omega)$ such that:

$$a(u, v) = (f, v) \quad \forall v \in \mathcal{V} \quad (21)$$

where (\cdot, \cdot) represents the scalar product in L^2 and $a(u, v) = (\nabla u, \nabla v)$. The following expressions are used for the respective methods, viz., the FEM, the SFEM and the VEM, to compute the stiffness matrix:

- $\mathbf{K}^{\text{FEM}} = \int_{\Omega} \mathbf{B}^T \mathbf{B} \, d\Omega.$

- $\mathbf{K}^{\text{SFEM}} = \sum_{C=1}^{nc} \int_{\Omega_C} \tilde{\mathbf{B}}_C^T \tilde{\mathbf{B}}_C \, d\Omega$
- $\mathbf{K}^{\text{VEM}} = \frac{\mathbf{R}\mathbf{R}^T}{|\Omega_e|} + (\mathbf{I} - \mathbf{\Pi})^T (\mathbf{I} - \mathbf{\Pi})$

where \mathbf{B} is the strain displacement matrix and $\tilde{\mathbf{B}}$ is the smoothed strain-displacement matrix given by:

$$\begin{aligned} \mathbf{B} &= \begin{bmatrix} \frac{\partial N_I}{\partial x} & \frac{\partial N_I}{\partial y} \end{bmatrix} \\ \tilde{\mathbf{B}} &= \frac{1}{A_C} \int_{S_C} \mathbf{n}^T N_I(\mathbf{x}) \, dS \end{aligned} \quad (22)$$

and $\mathbf{\Pi} = \tilde{\mathbf{\Pi}} + \mathbf{\Pi}_o(\mathbf{I} - \tilde{\mathbf{\Pi}})$ and $|\Omega_e| \tilde{\mathbf{\Pi}} = \mathbf{N}\mathbf{R}^T$. The matrices \mathbf{R} and \mathbf{N} are given by [18, 42]:

$$\mathbf{R} = \frac{1}{2} \begin{bmatrix} \ell_n \mathbf{n}_n + \ell_1 \mathbf{n}_1 \\ \ell_1 \mathbf{n}_1 + \ell_2 \mathbf{n}_2 \\ \dots \ell_{n-1} \mathbf{n}_{n-1} + \ell_n \mathbf{n}_n \end{bmatrix} \quad \mathbf{N} = \begin{bmatrix} x_1 & y_1 \\ x_2 & y_2 \\ \dots & \dots \\ x_n & y_n \end{bmatrix}$$

where $\ell_i (i = 1, \dots, n)$ is the length of edge i , x_n, y_n are the coordinates of the vertex of the polygon, $|\Omega_e|$ is the measure of the polygon.

4.1. Stiffness matrix for the unit square

In this case, consider a unit square $[0, 1] \times [0, 1]$. We compute the stiffness matrix using the conventional FEM with bilinear shape functions, the VEM and the SFEM with one and many subcells.

Finite element The stiffness matrix computed from the classical bilinear finite elements with reduced integration (i.e., one gauss point at the center of the element) and full integral (four gauss points):

$$\mathbf{K}_{\text{red}}^{\text{FEM}} = \frac{1}{2} \begin{bmatrix} 1 & 0 & -1 & 0 \\ 0 & 1 & 0 & -1 \\ -1 & 0 & 1 & 0 \\ 0 & -1 & 0 & 1 \end{bmatrix} \quad \mathbf{K}_{\text{full}}^{\text{FEM}} = \frac{1}{12} \begin{bmatrix} 8 & -2 & -4 & -2 \\ -2 & 8 & -2 & -4 \\ -4 & -2 & 8 & -2 \\ -2 & -4 & -2 & 8 \end{bmatrix} \quad (23)$$

Virtual element In this case, we use the order of the monomial $k = 1$. This implies that the shape functions on the boundary of the elements are linear. As noted in Section 3, the stiffness matrix computed from the VEM has two parts (see Equation (14)): (a) the consistency term and (b) the stability term. The consistency and the stability term are given by:

$$\mathbf{K}_{\text{const}}^{\text{VEM}} = \frac{1}{2} \begin{bmatrix} 1 & 0 & -1 & 0 \\ 0 & 1 & 0 & -1 \\ -1 & 0 & 1 & 0 \\ 0 & -1 & 0 & 1 \end{bmatrix} \quad \mathbf{K}_{\text{stab}}^{\text{VEM}} = \frac{1}{4} \begin{bmatrix} 1 & -1 & 1 & -1 \\ -1 & 1 & -1 & 1 \\ 1 & -1 & 1 & -1 \\ -1 & 1 & -1 & 1 \end{bmatrix} \quad (24)$$

and the final stiffness matrix is computed by adding the consistency term and the stability term:

$$\mathbf{K}^{\text{VEM}} = \frac{1}{12} \begin{bmatrix} 9 & -3 & -3 & -3 \\ -3 & 9 & -3 & -3 \\ -3 & -3 & 9 & -3 \\ -3 & -3 & -3 & 9 \end{bmatrix} \quad (25)$$

SFEM In this case, we use one and two subcells. The stiffness matrix with one subcell and two subcells are given by:

$$\mathbf{K}_{SC1Q4}^{SFEM} = \frac{1}{2} \begin{bmatrix} 1 & 0 & -1 & 0 \\ 0 & 1 & 0 & -1 \\ -1 & 0 & 1 & 0 \\ 0 & -1 & 0 & 1 \end{bmatrix} \quad \mathbf{K}_{SC2Q4}^{SFEM} = \frac{1}{16} \begin{bmatrix} 9 & -1 & -7 & -1 \\ -1 & 9 & -1 & -7 \\ -7 & -1 & 9 & -1 \\ -1 & -7 & -1 & 9 \end{bmatrix} \quad (26)$$

4.2. Stiffness matrix for the pentagon

The coordinates of the pentagon are: $[(0, 0), (3, 0), (3, 2), (3/2, 4), (0, 4)]$. The consistency and the stability term for the VEM are given by:

$$\mathbf{K}_{const}^{VEM} = \begin{bmatrix} 0.5952 & 0.0238 & -0.4881 & -0.4048 & 0.2738 \\ 0.0238 & 0.3095 & 0.0833 & -0.1190 & -0.2976 \\ -0.4881 & 0.0833 & 0.4345 & 0.2976 & -0.3274 \\ -0.4048 & -0.1190 & 0.2976 & 0.3095 & -0.0833 \\ 0.2738 & -0.2976 & -0.3274 & -0.0833 & 0.4345 \end{bmatrix}$$

$$\mathbf{K}_{stab}^{VEM} = \begin{bmatrix} 0.7422 & -0.1966 & -0.3412 & -0.2578 & 0.0534 \\ -0.1966 & 0.7422 & -0.3412 & -0.1354 & -0.0690 \\ -0.3412 & -0.3412 & 0.9896 & 0.0364 & -0.3437 \\ -0.2578 & -0.1354 & 0.0364 & 0.8646 & -0.5078 \\ 0.0534 & -0.0690 & -0.3437 & -0.5078 & 0.8672 \end{bmatrix} \quad (27)$$

and the stiffness matrix computed by employing the smoothing technique over the pentagon with one subcell is:

$$\mathbf{K}_{onecell}^{SFEM} = \begin{bmatrix} 0.5952 & 0.0238 & -0.4881 & -0.4048 & 0.2738 \\ 0.0238 & 0.3095 & 0.0833 & -0.1190 & -0.2976 \\ -0.4881 & 0.0833 & 0.4345 & 0.2976 & -0.3274 \\ -0.4048 & -0.1190 & 0.2976 & 0.3095 & -0.0833 \\ 0.2738 & -0.2976 & -0.3274 & -0.0833 & 0.4345 \end{bmatrix} \quad (28)$$

From the two examples, presented above, it can be observed that the consistency term of the VEM, stiffness matrix using SFEM with one subcell coincide with the conventional FEM with reduced integration. However, after the addition of the stability term in the VEM or increasing the number of subcells in the SFEM, we observe that the stiffness matrix computed from these approaches are different. It is also noted that the consistency term of the VEM is similar to the SFEM with one subcell. This observation also true in the case of the pentagon.

The SFEM starts with an assumption that the strain is constant within the subcell and then employs the divergence theorem to convert the domain integral into a surface integral. This alleviates the need to compute the derivatives of the shape functions and the stiffness matrix is computed from the information available on the boundary. When linear elements are employed on the boundary, this assumption holds true. However, when higher order elements are employed, this assumption breaks down. This was observed in [29], when the strain smoothing technique was employed to Q8 and Q9.

In the case of the VEM, no such assumption of constant strain is made over the element. However, the method starts by assuming the variation of the shape functions on the boundary of element. The method then employs divergence theorem after defining the projection operators [48, 42]. Hence, when linear variation is assumed, the VEM with consistency term and the SFEM with one subcell coincide. This is also true when the number of sides is > 4 , as noted in the previous example. The stiffness matrix of the VEM has two parts: (a) the first term ensures *consistency* and this term must be computed exactly and (b) the second term ensures *stability*, this can be approximated. The important features of the stability term are: (a) it should scale like the consistency term and (b) should be positive definite. Different choices of stability term is possible as discussed in [48, 49, 44].

However, for this study, we employ the following stability term based on the work of Beirão Da Veiga *et al.*, [48, 49]:

$$\mathbf{K}_2 = \alpha \mathbf{P} \quad (29)$$

where $\alpha = \alpha^* \text{trace}(\mathbf{K}_{\text{const}}^{\text{VEM}})$ and \mathbf{P} is the orthogonal projection operation and is chosen as:

$$\mathbf{P} = \mathbf{I} - \mathbf{T} (\mathbf{T}^T \mathbf{T})^{-1} \mathbf{T}^T \quad (30)$$

and the matrix \mathbf{T} is the modified nodal coordinate matrix N of dimension $3n \times 12$ in the case of 3D:

$$T_{3I-2:3I} = \begin{bmatrix} 1 & 0 & 0 & y_I & 0 & -z_I & x_I & 0 & 0 & y_I & 0 & z_I \\ 0 & 1 & 0 & -x_I & z_I & 0 & 0 & y_I & 0 & x_I & z_I & 0 \\ 0 & 0 & 1 & 0 & -y_I & x_I & 0 & 0 & z_I & 0 & y_I & x_I \end{bmatrix} \quad (31)$$

where α^* is a scaling coefficient chosen based on a parametric study conducted in the next section. We conclude that the CSFEM is a special case of the more general VEM. Instead of increasing the number of subcells, we add to the one-subcell, the stability term borrowed from the VEM. In this present study, we employ the following form for the stiffness matrix:

$$\mathbf{K}^h = \mathbf{K}_1 + \mathbf{K}_2 \quad (32)$$

where

$$\mathbf{K}_1 = \int_{\Omega_C} \tilde{\mathbf{B}}_C^T \mathbf{D} \tilde{\mathbf{B}}_C \, d\Omega \quad (33)$$

is computed by employing the strain smoothing technique and

$$\mathbf{K}_2 = \alpha \mathbf{P} \quad (34)$$

Since the consistency term of the VEM and the SFEM with one subcell are identical, we have $\alpha = \alpha^* \text{trace}(\mathbf{K}_1)$.

5. NUMERICAL EXAMPLES

In the first part of this section, we employ the cell-based smoothed finite element method with new stabilization approach to two-dimensional benchmark problems in linear elasticity. The results from the new approach are compared with analytical solution where available and with the conventional FEM. The SFEM with stabilization is applied to polygonal elements in 2D and the accuracy and the convergence properties are studied in detail. Later, the proposed SFEM with stabilization is extended to 3D problems with hexahedral and polyhedral elements. Again, the accuracy and the convergence properties of the proposed method are studied with a patch test and a cantilever beam loaded in shear. In the last part of the section, the SFEM is combined with the scaled boundary FEM to problems involving strong discontinuity and singularities. The results are compared with available solutions in the literature.

The built-in Matlab[®] function `voronoin` and Matlab[®] functions in PolyTop [50] for building mesh-connectivity are used to create the polygonal meshes. For polyhedra mesh, the open source software Neper [51] is employed for building the mesh-connectivity. For the purpose of error estimation and convergence studies, the error, L^2 and H^1 norms are used. The displacement norm is given by:

$$\|\mathbf{u} - \mathbf{u}^h\|_{L^2(\Omega)} = \sqrt{\int_{\Omega} [(\mathbf{u} - \mathbf{u}^h) \cdot (\mathbf{u} - \mathbf{u}^h)] \, d\Omega} \quad (35)$$

where \mathbf{u}^h is the numerical solution and \mathbf{u} is the analytical or a reference solution. The energy norm is given by:

$$\|\mathbf{u} - \mathbf{u}^h\|_{H^1(\Omega)} = \sqrt{\int_{\Omega} [(\boldsymbol{\varepsilon} - \boldsymbol{\varepsilon}^h) \mathbf{D} (\boldsymbol{\varepsilon} - \boldsymbol{\varepsilon}^h)] \, d\Omega} \quad (36)$$

5.1. Applications to two dimensional problems

5.1.1. Cantilever beam A two-dimensional cantilever beam subjected to a parabolic shear load at the free end is examined as shown in Figure (8). The geometry is: length $L = 8$, height $D = 4$. The material properties are: Young's modulus, $E = 3e^7$, Poisson's ratio $\nu = 0.3$ and the parabolic shear force $P = 250$. The exact solution for displacements are given by:

$$\begin{aligned} u(x, y) &= \frac{Py}{6\bar{E}I} \left[(9L - 3x)x + (2 + \bar{\nu}) \left(y^2 - \frac{D^2}{4} \right) \right] \\ v(x, y) &= -\frac{P}{6\bar{E}I} \left[3\bar{\nu}y^2(L - x) + (4 + 5\bar{\nu})\frac{D^2x}{4} + (3L - x)x^2 \right] \end{aligned} \quad (37)$$

where $I = D^3/12$ is the moment of inertia, $\bar{E} = E$, $\bar{\nu} = \nu$ and $\bar{E} = E/(1 - \nu^2)$, $\bar{\nu} = \nu/(1 - \nu)$ for plane stress and plane strain, respectively. The domain is discretized with two different mesh types: (a) structured quadrilateral elements (8×4 , 16×8 , 32×16 , 64×32) and (b) polygonal elements. Figure (7) shows a sample polygonal mesh used for this study. Before demonstrating the convergence and the accuracy of the SFEM with stabilization, we investigate the influence of the scaling parameter α^* . Figure (10) shows the influence of the scaling parameter α on the relative error in the L^2 and H^1 norm. It is observed that the relative error attains a minimum value for $\alpha^* = 0.1$.

The numerical convergence of the relative error in the displacement norm and the relative error in the energy norm is shown in Figure (10) for structured quadrilateral elements. The problem is solved with conventional SFEM with one (SC1Q4) and two subcells (SC2Q4) and with the proposed SFEM with and without stabilization. It is observed that the SC1Q4 and SFEM with no stabilization yield similar results, as seen in the scalar example in Section 4. However, the SC2Q4 and SFEM with stabilization yield different results. This can be attributed to the choice of the scaling parameter α^* . It can be seen that with mesh refinement, all the approaches converge with optimal rate. For the choice of α^* , it is seen that SFEM with stabilization yields more accurate results than the SC2Q4.

Figure (11) shows the convergence of the displacement and the energy norm with mesh refinement. In this case, one subcell per polygonal element cannot be used, as it has spurious energy modes [37]. Hence, in this study, for the conventional SFEM and the FEM, we sub-triangulate the polygonal element and integrate over each sub-triangle. In the case of the proposed approach, we employ one subcell and add the stabilization term (Equation (29)). It can be observed that the proposed SFEM with stabilization yields more accurate results when compared to conventional SFEM with triangulation.

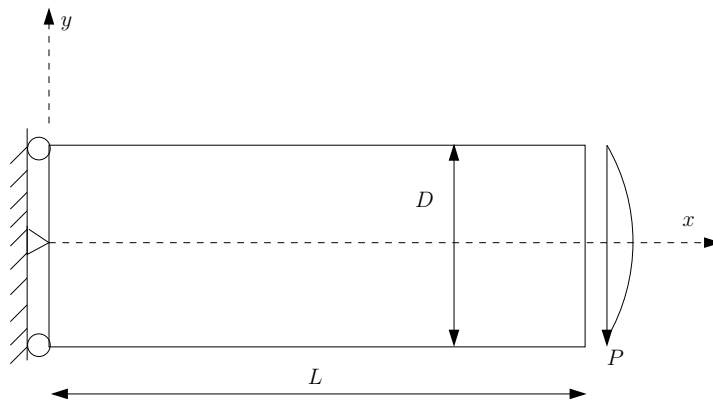


Figure 7. Cantilever beam: Geometry and boundary conditions.

5.1.2. Infinite plate with a circular hole In this example, consider an infinite plate with a traction free hole under uniaxial tension ($\sigma = 1$) along x -axis Figure (12). The exact solution of the principal

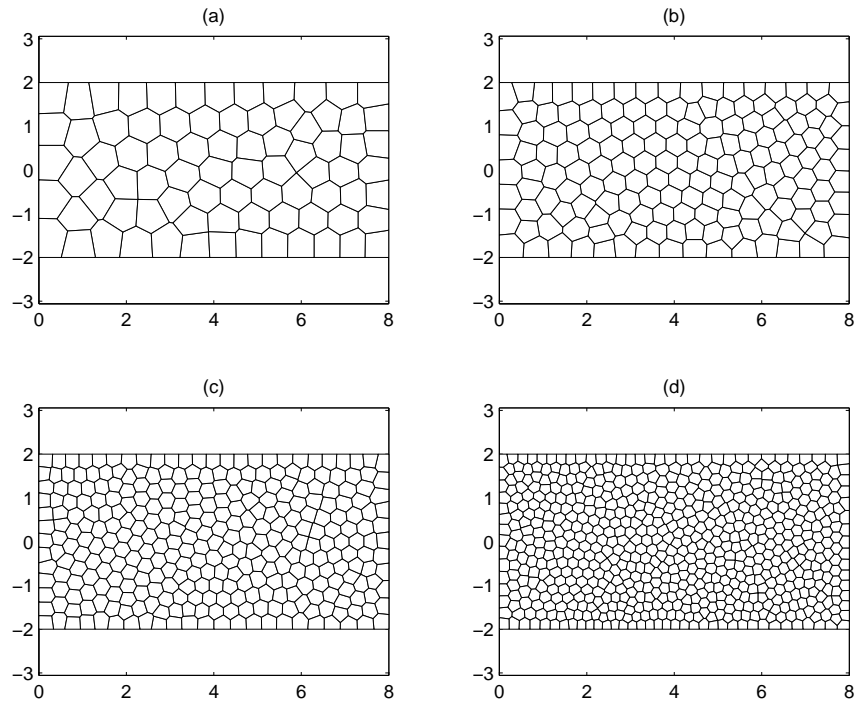


Figure 8. Cantilever beam: Typical polygonal mesh employed in this study.

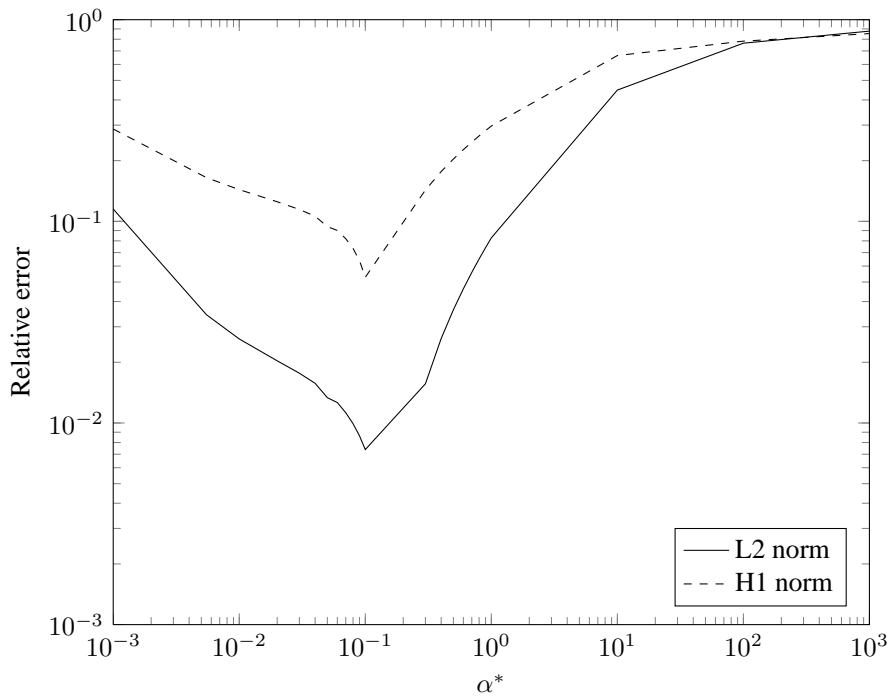
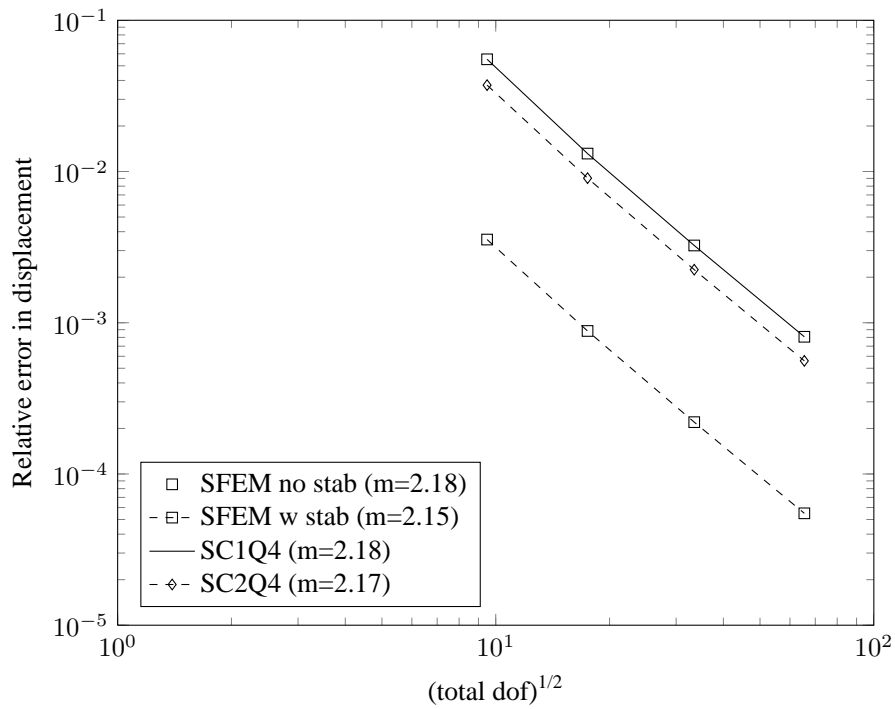
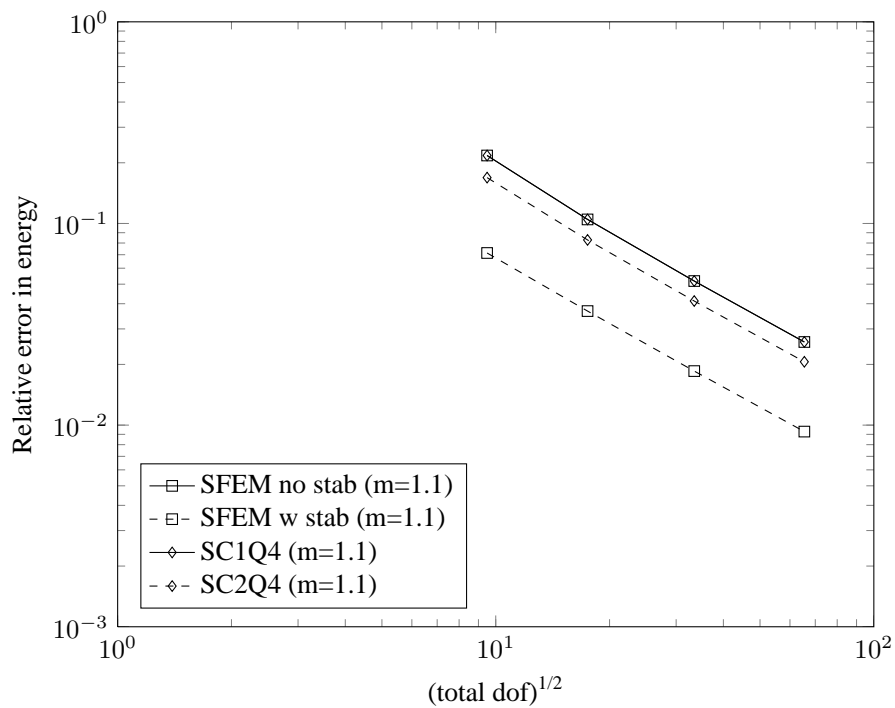


Figure 9. Bending of thick cantilever beam: Influence of α^* .

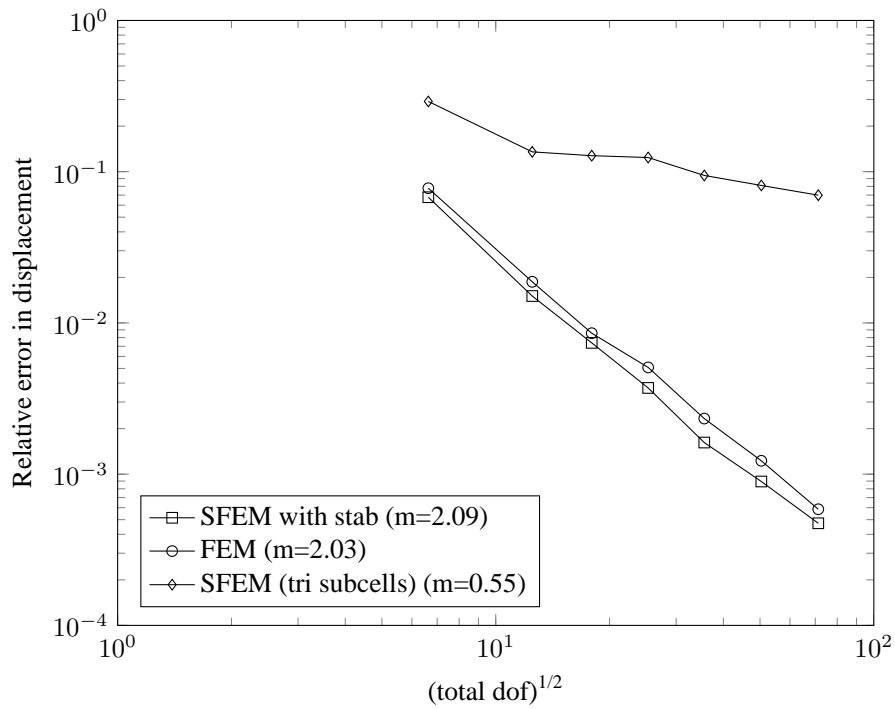


(a)

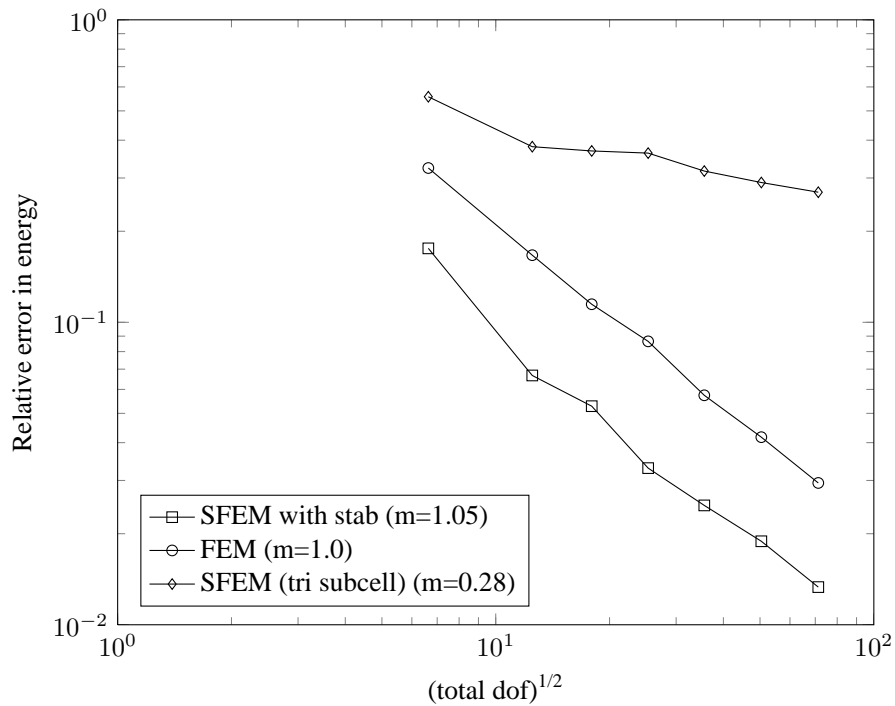


(b)

Figure 10. Bending of thick cantilever beam: Convergence results for (a) the relative error in the displacement norm (L^2) and (b) the relative error in the energy norm. The rate of convergence is also shown, where m is the average slope. The domain is discretized with Q4 elements.



(a)



(b)

Figure 11. Bending of thick cantilever beam: Convergence results for (a) the relative error in the displacement norm (L^2) and (b) the relative error in the energy norm. The rate of convergence is also shown, where m is the average slope. The domain is discretized with arbitrary polygonal elements.

stresses in polar coordinates (r, θ) is given by:

$$\begin{aligned}\sigma_{11}(r, \theta) &= 1 - \frac{a^2}{r^2} \left(\frac{3}{2}(\cos 2\theta + \cos 4\theta) \right) + \frac{3a^4}{2r^4} \cos 4\theta \\ \sigma_{22}(r, \theta) &= -\frac{a^2}{r^2} \left(\frac{1}{2}(\cos 2\theta - \cos 4\theta) \right) - \frac{3a^4}{2r^4} \cos 4\theta \\ \sigma_{12}(r, \theta) &= -\frac{a^2}{r^2} \left(\frac{1}{2}(\sin 2\theta + \sin 4\theta) \right) + \frac{3a^4}{2r^4} \sin 4\theta\end{aligned}\quad (38)$$

where a is the radius of the hole. Owing to symmetry, only one quarter of the plate is modeled. Figure (13) shows a typical polygonal mesh used for the study. The material properties are: Young's modulus $E = 10^5$ and Poisson's ratio $\nu = 0.3$. In this example, analytical tractions are applied on the boundary. The domain is discretized with polygonal elements and along each edge of the polygon, the shape function is linear. The convergence rate in terms of the displacement norm is shown in Figure (14). It is observed that the proposed method yields more accurate results when compared to the conventional SFEM with triangular subcells. For the present study, the scaling coefficient α^* is taken as 0.1.

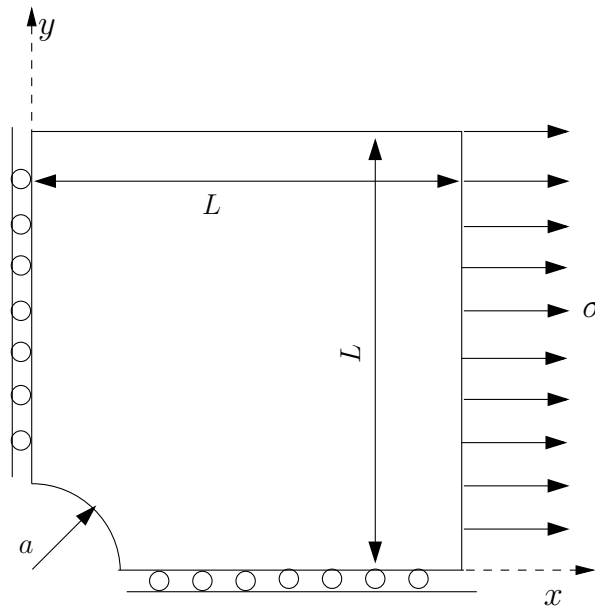


Figure 12. Infinite plate with a circular hole.

5.1.3. L-shaped domain under mode I loading In this example, consider the singular problem of a finite portion of an infinite domain with a reentrant corner. The model is loaded on part of the boundary, which is indicated by discontinuous thick lines in Figure 15. The tractions correspond to the first terms of the asymptotic expansion that describes the exact solution under mixed mode loading conditions around the singular vertex. The exact displacement and stress fields for this singular elasticity problem can be found in [52]. Exact values of the generalised stress intensity factors (GSIF) [52] under mode I were taken as $K_I = 1$ and $K_{II} = 0$. The material parameters are Young's modulus $E = 1000$, and Poisson's ratio $\nu = 0.3$ and the domain is discretized with polygonal elements. The problem is solved by the conventional polygonal FEM and the SFEM with stabilization. The convergence of the relative error in displacement with mesh refinement is shown in Figure (16). It is observed that both the approaches converge with mesh refinement, however, the SFEM with stabilization yields more accurate results. It is noted that since the domain has a reentrant corner, the optimal convergence rate is not achieved.

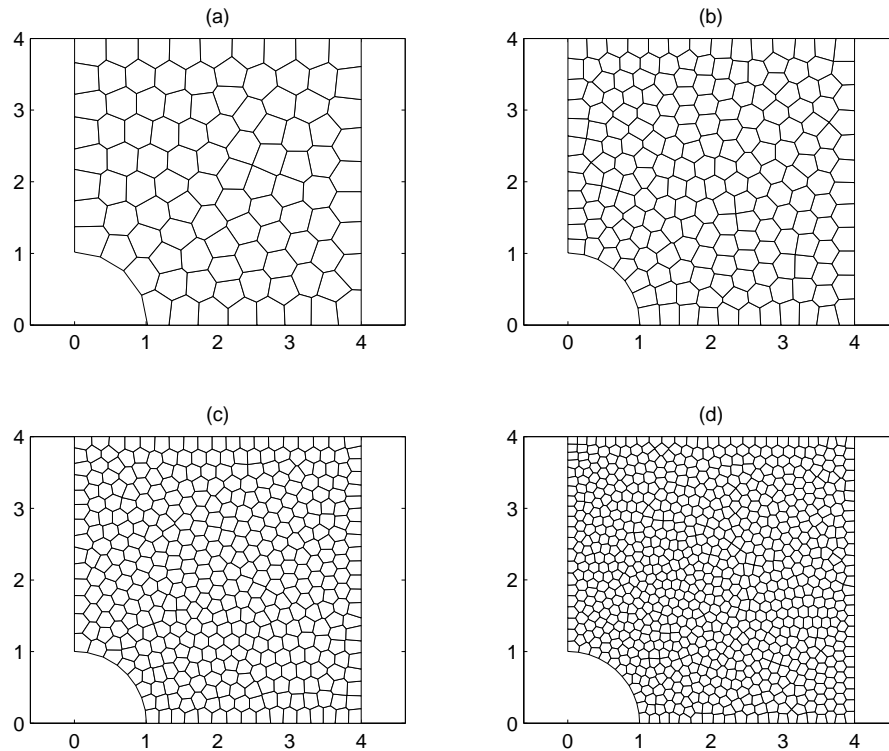


Figure 13. Plate with a circular hole: domain discretized with polygonal elements: (a) 100 elements; (b) 200 elements; (c) 400 elements and (d) 800 elements.

5.2. Applications to three dimensional problems

5.2.1. Stability condition Before we proceed to study the accuracy and the convergence of the proposed method, we first investigate the stability condition by computing the eigenvalues of the hexahedral element shown in Figure (17). The eigenvalues of the stiffness matrix computed by using the trilinear shape functions are $\lambda = \{0, 0, 0, 0, 0, 0, 1.47, 3.11, 3.55, 4.28, 4.82, 6.04, 6.44, 6.98, 8.75, 9.85, 11.50, 12.75, 13.34, 14.19, 15.06, 16.24, 16.62, 45.91\}$. We solve the same problem with the proposed SFEM with and without stabilization. The eigenvalues of the stiffness matrix computed by SFEM without stabilization (i.e., with one subcell are): $\lambda = \{0, 0, 0, 0, 0, 0, 0, 0, 0, 0, 0, 0, 0, 0, 0, 0, 9.92, 11.64, 13.60, 16.37, 16.62, 46.98\}$ and with stabilization ($\alpha = 0.1$) are: $\lambda = \{0, 0, 0, 0, 0, 0, 9.32, 9.45, 10.42, 10.64, 11.30, 11.49, 11.51, 11.51, 11.51, 11.51, 11.51, 11.53, 12.41, 15.09, 17.36, 17.72, 47.45\}$ It can be seen that SFEM with stabilization, like the FEM can capture the six zero energy modes corresponding to the physical rigid body modes. This indicates that the stiffness matrix is full rank and does not have any spurious energy modes. However, with one subcell and without stabilization, the eigenvalues of the stiffness matrix has 12 additional zero energy modes, these are non-physical. This is identical to the FEM with one integration point. Traditionally, for hexahedral elements, these are suppressed by stabilization procedures. In [53, 54], the authors suppresses the zero energy modes, by adding the stiffness matrix computed with 8 subcells. In the present study, we add the stability term as given by Equation (29).

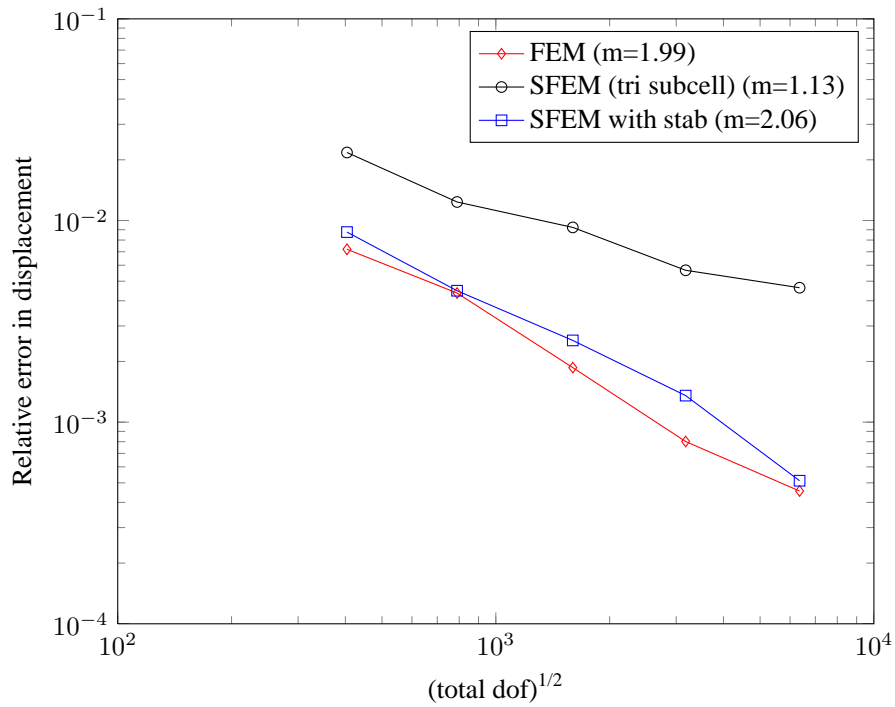


Figure 14. Infinite plate with a circular hole: Convergence results for the relative error in the displacement norm (L^2). The rate of convergence is also shown, where m is the average slope.

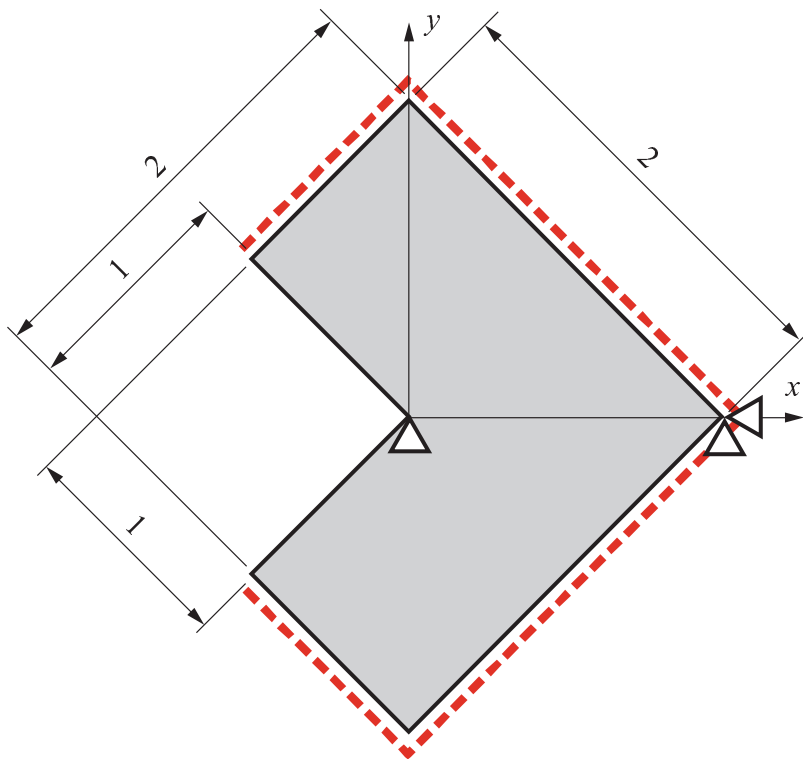


Figure 15. L-shaped domain.

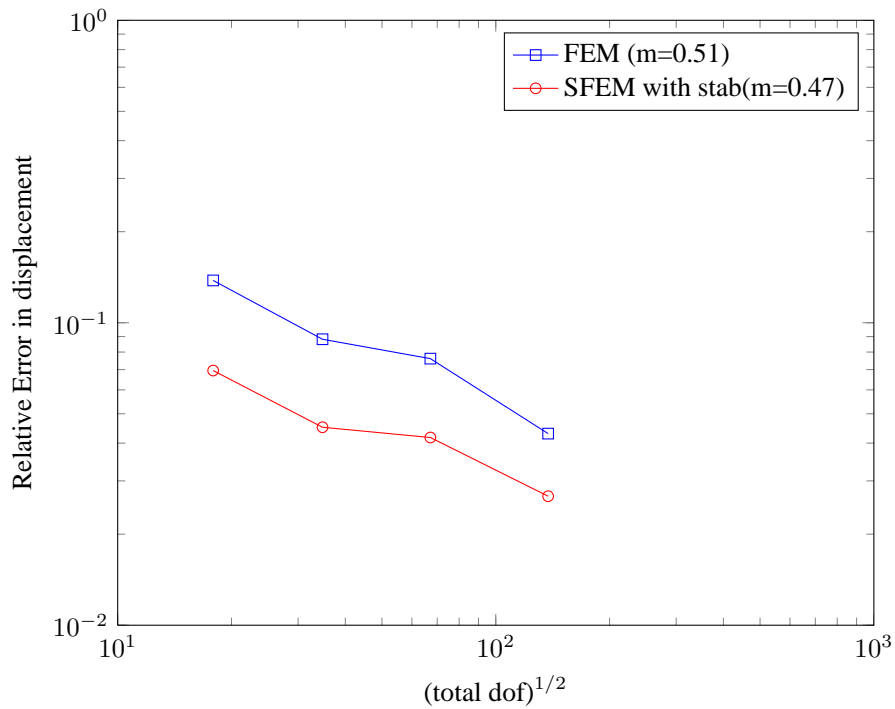


Figure 16. L-shaped domain under mode I loading: Convergence results for the relative error in the displacement norm (L^2). The rate of convergence is also shown, where m is the average slope.

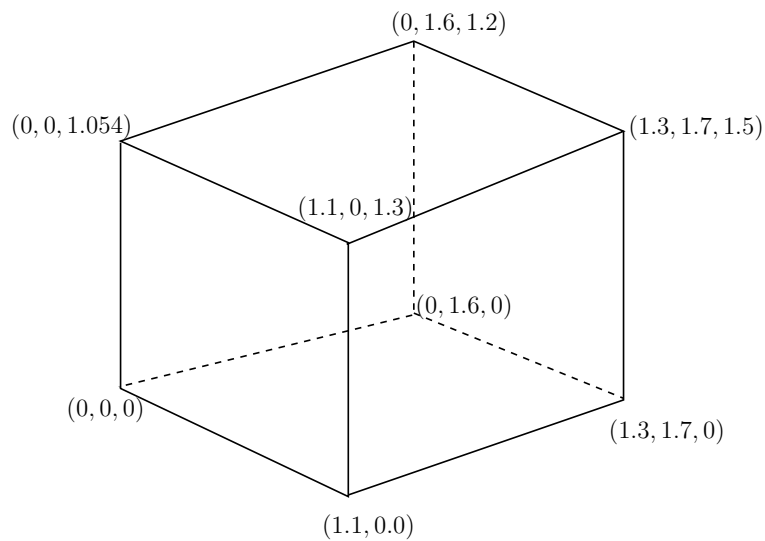


Figure 17. Hexahedral element for the stability test

5.2.2. *Patch Test* A three dimensional patch test with warped elements suggest in [55] is considered. The patch of elements shown in Figure (18) is tested with the following displacement

field applied on the outer boundary:

$$\begin{aligned} u &= \frac{1}{2}(2x + y + z)10^{-3} \\ v &= \frac{1}{2}(x + 2y + z)10^{-3} \\ w &= \frac{1}{2}(x + y + 2z)10^{-3} \end{aligned} \quad (39)$$

The coordinates of the interior nodes are given in Table I. The interior nodes are enclosed within a unit cube. It is observed that both the FEM with $3 \times 3 \times 3$ Gaussian quadrature and cell-based smoothed technique with stabilization pass the patch test to machine precision.

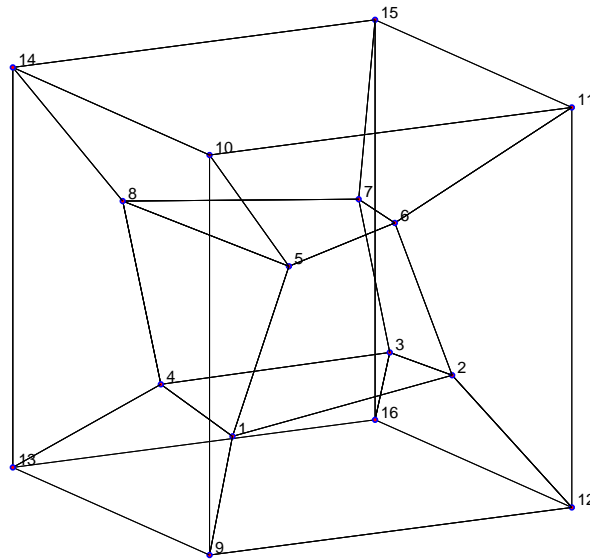


Figure 18. Mesh used for displacement patch test: a cube containing warped elements (the coordinates of the interior nodes are given in Table I).

Table I. Three dimensional patch test: coordinates of inner nodes. The inner nodes are enclosed within a unit cube [55].

Node number	x	y	z
1	0.249	0.342	0.192
2	0.826	0.288	0.288
3	0.850	0.649	0.263
4	0.273	0.750	0.230
5	0.320	0.186	0.643
6	0.677	0.305	0.683
7	0.788	0.693	0.644
8	0.165	0.745	0.705

5.2.3. *Cantilever beam under shear load* Consider a cantilever beam loaded in shear. The domain Ω for this problem is $[-1, 1] \times [-1, 1] \times [0, L]$. The material is assumed to be isotropic with Young's

modulus, $E = 1 \text{ N/m}^2$ and Poisson's ratio $\nu = 0.3$. The beam is subjected to a shear force F at $z = L$ and at any cross section of the beam, we have:

$$\int_{-a}^b \int_{-a}^b \sigma_{yz} \, dx dy = F \quad \int_{-a}^b \int_{-a}^b \sigma_{zz} y \, dx dy = Fz \quad (40)$$

The Cauchy stress field is given by [56]:

$$\begin{aligned} \sigma_{xx} &= \sigma_{xy} = \sigma_{yy} = 0 \\ \sigma_{zz} &= \frac{F}{I} yz \\ \sigma_{xz} &= \frac{2a^2 \nu F}{\pi^2 I (1 + \nu)} \sum_{n=0}^{\infty} \frac{(-1)^n}{n^2} \sin\left(\frac{n\pi x}{a}\right) \frac{\sinh\left(\frac{n\pi y}{a}\right)}{\cosh\left(\frac{n\pi b}{a}\right)} \\ \sigma_{yz} &= \frac{(b^2 - y^2)F}{2I} + \frac{\nu F}{I(1 + \nu)} \left[\frac{3x^2 - a^2}{6} - \frac{2a^2}{\pi^2} \sum_{n=1}^{\infty} \frac{(-1)^n}{n^2} \cos\left(\frac{n\pi x}{a}\right) \frac{\cosh\left(\frac{n\pi y}{a}\right)}{\cosh\left(\frac{n\pi b}{a}\right)} \right] \end{aligned} \quad (41)$$

The corresponding displacement field is given by [57]:

$$\begin{aligned} u &= -\frac{\nu F}{EI} xyz \\ v &= \frac{F}{EI} \left[\frac{\nu(x^2 - y^2)z}{2} - \frac{z^3}{6} \right] \\ w &= \frac{F}{EI} \left[\frac{y(\nu x^2 + z^2)}{2} + \frac{\nu y^3}{6} + (1 + \nu) \left(b^2 y - \frac{y^3}{3} \right) - \frac{\nu a^2 y}{3} - \frac{4\nu a^3}{\pi^3} \sum_{n=0}^{\infty} \frac{(-1)^n}{n^2} \cos\left(\frac{n\pi x}{a}\right) \frac{\sinh\left(\frac{n\pi y}{a}\right)}{\cosh\left(\frac{n\pi b}{a}\right)} \right] \end{aligned} \quad (42)$$

where E is the Young's modulus, ν is Poisson's ratio and $I = 4ab^3/3$ is the second moment of area about the x -axis. Two type of meshes are considered: (a) a regular hexahedral mesh and (2) a random closed -pack Voronoi mesh. Four levels of mesh refinement are considered for both hexahedral mesh ($2 \times 2 \times 10$, $4 \times 4 \times 20$, $8 \times 8 \times 40$, $16 \times 16 \times 80$) and for random Voronoi mesh. Figure (20) shows the random Voronoi mesh employed for this study. The length of the beam is $L = 5$ and the shear load is taken as $F = 1$. Analytical displacements given by Equation (42) are applied at $z = L$, whilst the beam is loaded in shear at $z = 0$. All other faces are assumed to be traction free. Figure (21) shows the relative error in the displacement norm with mesh refinement. It can be seen that both the formulations, viz., FEM and SFEM with stabilization converge to analytical solution with mesh refinement. It is also observed that the SFEM with stabilization yields slightly more accurate results when compared to the FEM with full integration. Also, shown in Figure (21) is the convergence of the method with polyhedra meshes. Although, the formulation when applied to polyhedra elements, converge with mesh refinement, it is not as accurate as the hexahedral elements. This can attributed to the parameter α^* employed in this study and this observation is consistent with the results reported in the literature [44].

5.3. Application to linear elastic fracture mechanics

The SFEM with stabilization discussed above over arbitrary polygons and polyhedrons can be applied to problems with strong discontinuity and singularity. However, to accurately capture the asymptotic fields at the crack tip, a very fine mesh in combination with singular elements at the crack tip is usually required. This poses additional difficulties when the crack evolves. Another possibility is to enrich the approximation space with functions that can capture the discontinuity and singularity [4, 5]. In the literature, the latter method is referred to as the Generalized FEM (GFEM)/extended finite element method (XFEM). In [29], the authors combined the strain smoothing with the XFEM. It was observed that in the case of enrichment schemes for linear elastic

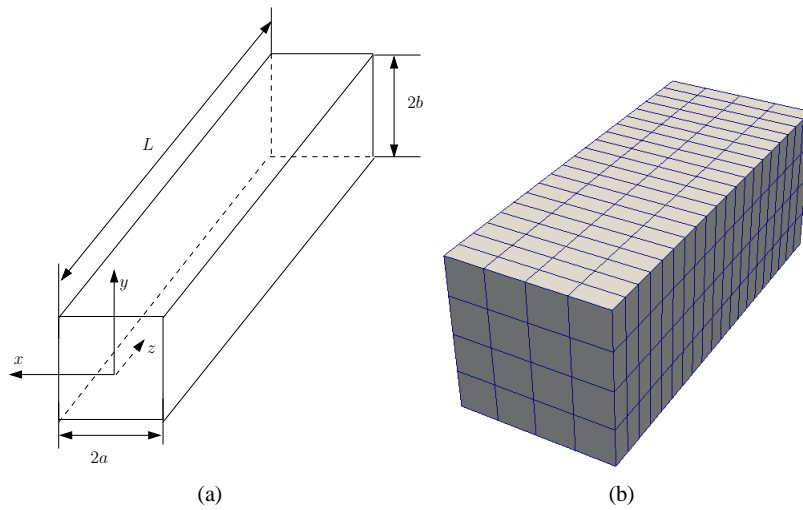


Figure 19. Cantilever beam: (a) Geometry, length L and rectangular cross-section of width $2a$ and height $2b$. For the present study, the following dimensions are considered: $L = 5$, $a = b = 1$ and (b) A structured hexahedral mesh ($4 \times 4 \times 20$).

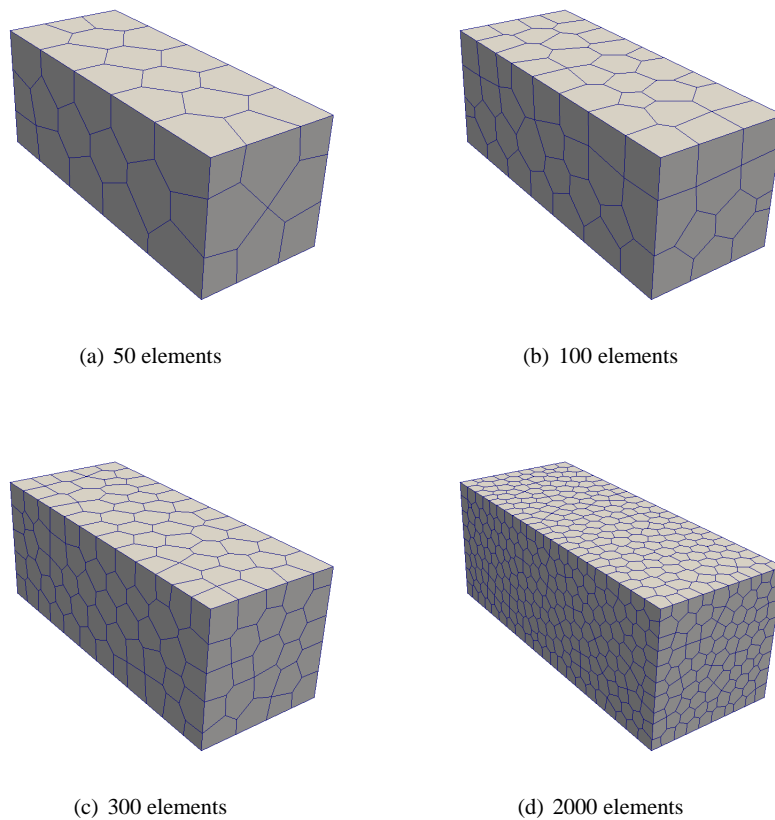


Figure 20. Random closed pack centroid Voronoi tessellation.

fracture mechanics, the method yielded less accurate results compared to the conventional XFEM.

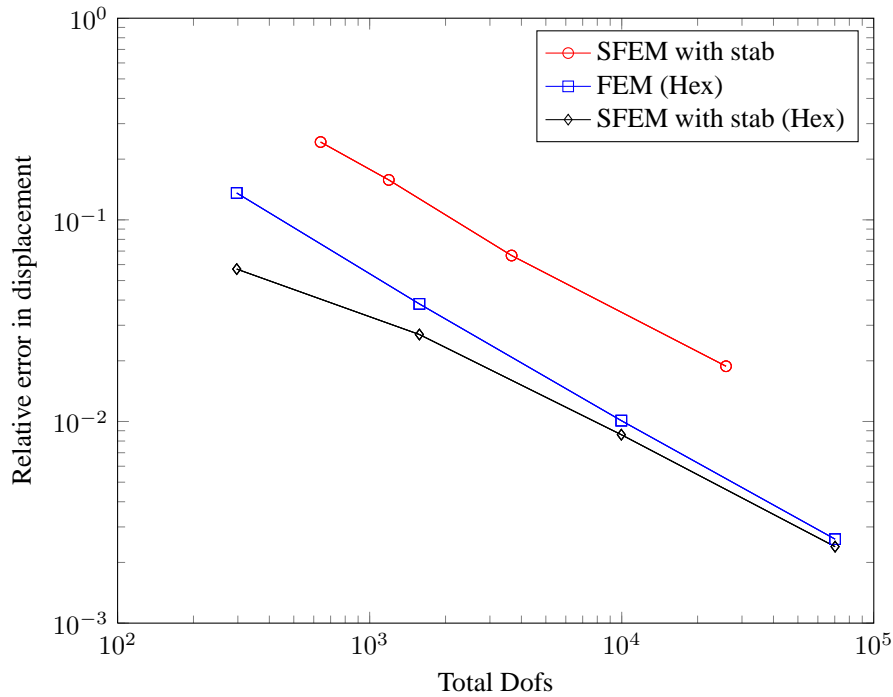


Figure 21. Beam with shear load: convergence of the relative error in the displacement.

However, for the elements that are completely intersected by the discontinuous surface, with the strain smoothing operation, further sub-division is not required.

In this study, we propose to couple the SFEM with the scaled boundary finite element method (SBFEM) to model problems with strong discontinuity and singularities. The SBFEM is a novel method that has the advantages of the FEM and the boundary element method (BEM). Like the FEM, no fundamental solution is required and like the BEM, the problem dimension is reduced by one. The SBFEM is a semi-analytical method and relies on defining a ‘scaling centre’ from which the entire boundary is visible. This is similar to the concept of ‘star convexity’. The boundary is divided into conventional linear finite elements, whilst the solution is sought analytically in the radial direction [16]. Moreover, by exploiting the special characteristics of the scaling centre, the stress intensity factors can be computed directly. When modelling a crack/notched surface the scaling centre is placed at the crack tip. The straight crack/notch edges are formed by scaling the nodes A and B on the boundary and the crack surfaces are not discretized (see Figure (22)).

Displacement approximation The geometry of the element described by the coordinates on the boundary $\mathbf{x}_b(\eta)$ is expressed as:

$$\mathbf{x}_b(\eta) = \mathbf{N}(\eta)\mathbf{x}_b \quad (43)$$

where $\mathbf{N}(\eta)$ is the shape function matrix of the finite elements discretising the polygon boundary. The standard 1D Gauss-Lobatto shape functions or Lagrange shape functions can be used. In this study, we employ Lagrange shape functions. The displacements of a point in a polygon is approximated by:

$$\mathbf{u}(\xi, \eta) = \mathbf{N}(\eta)\mathbf{u}(\xi) \quad (44)$$

where $\mathbf{u}(\xi)$ are radial displacement functions. Substituting Equation (44) in the definition of strain-displacement relations, the strains $\boldsymbol{\varepsilon}(\xi, \eta)$ are expressed as:

$$\boldsymbol{\varepsilon}(\xi, \eta) = \mathbf{L}\mathbf{u}(\xi, \eta) \quad (45)$$

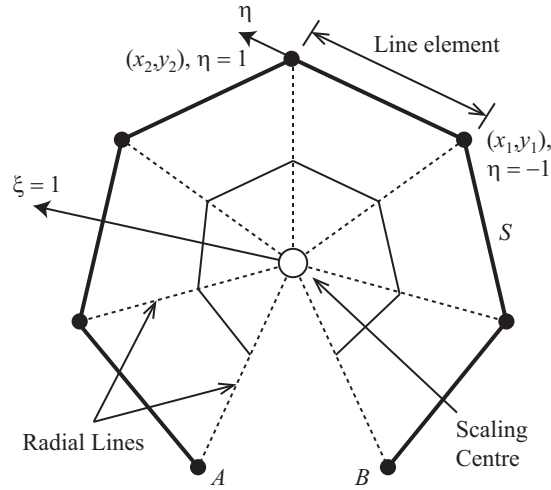


Figure 22. Cracked polygon representation by the scaled boundary finite element method.

where \mathbf{L} is a linear operator matrix formulated in the scaled boundary coordinates as

$$\mathbf{L} = \mathbf{b}_1(\eta) \frac{\partial}{\partial \xi} + \xi^{-1} \mathbf{b}_2(\eta) \quad (46)$$

with

$$\mathbf{b}_1(\eta) = \frac{1}{|\mathbf{J}(\eta)|} \begin{bmatrix} y_{\eta}(\eta)_{,\eta} & 0 \\ 0 & -x_{\eta}(\eta)_{,\eta} \\ -x_{\eta}(\eta)_{,\eta} & y_{\eta}(\eta)_{,\eta} \end{bmatrix}$$

$$\mathbf{b}_2(\eta) = \frac{1}{|\mathbf{J}(\eta)|} \begin{bmatrix} -y_{\eta}(\eta) & 0 \\ 0 & x_{\eta}(\eta) \\ x_{\eta}(\eta) & y_{\eta}(\eta) \end{bmatrix} \quad (47)$$

By following the procedure outlined in [58, 59], the following ODE is obtained:

$$\mathbf{E}_0 \xi^2 \mathbf{u}(\xi)_{,\xi\xi} + (\mathbf{E}_0 + \mathbf{E}_1^T - \mathbf{E}_1) \xi \mathbf{u}(\xi)_{,\xi} - \mathbf{E}_2 \mathbf{u}(\xi) = 0 \quad (48)$$

where \mathbf{E}_0 , \mathbf{E}_1 and \mathbf{E}_2 are coefficient matrices given by:

$$\mathbf{E}_0 = \int_{\eta} \mathbf{B}_1(\eta)^T \mathbf{D} \mathbf{B}_1(\eta) |\mathbf{J}(\eta)| d\eta,$$

$$\mathbf{E}_1 = \int_{\eta} \mathbf{B}_2(\eta)^T \mathbf{D} \mathbf{B}_1(\eta) |\mathbf{J}(\eta)| d\eta,$$

$$\mathbf{E}_2 = \int_{\eta} \mathbf{B}_2(\eta)^T \mathbf{D} \mathbf{B}_2(\eta) |\mathbf{J}(\eta)| d\eta. \quad (49)$$

Using Equation (45) and Hooke's law $\boldsymbol{\sigma} = \mathbf{D}\boldsymbol{\varepsilon}$, the stresses $\boldsymbol{\sigma}(\xi, \eta)$ is expressed as

$$\boldsymbol{\sigma}(\xi, \eta) = \mathbf{D} (\mathbf{B}_1(\eta) \mathbf{u}(\xi)_{,\xi} + \xi^{-1} \mathbf{B}_2(\eta) \mathbf{u}(\xi)) \quad (50)$$

where \mathbf{D} is the material constitutive matrix and the determinant of the Jacobian matrix is:

$$|\mathbf{J}(\eta)| = x_b(\eta) y_b(\eta)_{,\eta} - y_b(\eta) x_b(\eta)_{,\eta} \quad (51)$$

The coefficient matrices are evaluated element-by-element on the polygon boundary and assembled over a polygon. This process is similar to the standard FE procedure of assemblage. Equation (48) is

a homogeneous second-order ordinary differential equation. Its solution is obtained by introducing the variable $\chi(\xi)$

$$\chi(\xi) = \begin{Bmatrix} \mathbf{u}(\xi) \\ \mathbf{q}(\xi) \end{Bmatrix} \quad (52)$$

where $\mathbf{q}(\xi)$ is the internal load vector

$$\mathbf{q}(\xi) = \mathbf{E}_0 \xi \mathbf{u}(\xi)_{,\xi} + \mathbf{E}_1^T \mathbf{u}(\xi) \quad (53)$$

The boundary nodal forces are related to the displacement functions by:

$$\mathbf{f} = \mathbf{q}(\xi = 1) = (\mathbf{E}_0 \xi \mathbf{u}(\xi)_{,\xi} + \mathbf{E}_1^T \mathbf{u}(\xi))|_{\xi=1} \quad (54)$$

This allows Equation (48) to be transformed into a first order ordinary differential equation with twice the number of unknowns in an element as:

$$\xi \chi(\xi)_{,\xi} = -\mathbf{Z} \chi(\xi) \quad (55)$$

where \mathbf{Z} is a Hamiltonian matrix

$$\mathbf{Z} = \begin{bmatrix} \mathbf{E}_0^{-1} \mathbf{E}_1^T & -\mathbf{E}_0^{-1} \\ \mathbf{E}_1 \mathbf{E}_0^{-1} \mathbf{E}_1^T - \mathbf{E}_2 & -\mathbf{E}_1 \mathbf{E}_0^{-1} \end{bmatrix} \quad (56)$$

An eigenvalue decomposition of \mathbf{Z} is performed. The blocks of eigenvalues and transformation matrices necessary are:

$$\mathbf{Z} \begin{bmatrix} \Phi_u \\ \Phi_q \end{bmatrix} = \begin{bmatrix} \Phi_u \\ \Phi_q \end{bmatrix} \Lambda_n \quad (57)$$

In Equation (57), $\Lambda_n = \text{diag}(\lambda_1, \lambda_2, \dots, \lambda_n)$ contains the eigenvalues with negative real part. Φ_u and Φ_q are the corresponding transformation matrices of Λ_n . They represent the modal displacements and forces, respectively. The general solution of Equation (55) is given by:

$$\mathbf{u}(\xi) = \Phi_u \xi^{-\Lambda_n} \mathbf{c} \quad (58)$$

$$\mathbf{q}(\xi) = \Phi_q \xi^{-\Lambda_n} \mathbf{c} \quad (59)$$

where \mathbf{c} are integration constants that are obtained from the nodal displacements $\mathbf{u}_b = \mathbf{u}(\xi = 1)$ as:

$$\mathbf{c} = \Phi_u^{-1} \mathbf{u}_b \quad (60)$$

The complete displacement field of a point defined by the sector covered by a line element on the element is obtained by substituting Equation (59) into Equation (44) resulting in:

$$\mathbf{u}(\xi, \eta) = \mathbf{N}(\eta) \Phi_u \xi^{-\Lambda_n} \mathbf{c} \quad (61)$$

Taking the derivative of $\mathbf{u}(\xi)$ with respect to ξ and substituting into Equation (50) the stress field $\sigma(\xi, \eta)$ can be expressed as:

$$\sigma(\xi, \eta) = \Psi_\sigma(\eta) \xi^{-\Lambda_n - \mathbf{I}} \mathbf{c} \quad (62)$$

where the stress mode $\Psi_\sigma(\eta)$ is defined as:

$$\Psi_\sigma(\eta) = \mathbf{D} (-\mathbf{B}_1(\eta) \Phi_u \Lambda_n + \mathbf{B}_2(\eta) \Phi_u) \quad (63)$$

The stiffness matrix of an element is obtained by first substituting Equation (60) into Equation (59) at $\xi = 1$. This results in:

$$\mathbf{f} = \Phi_q \Phi_u^{-1} \mathbf{u}_b \quad (64)$$

From Equation (64), the stiffness matrix \mathbf{K} can be identified to be given by the expression

$$\mathbf{K} = \Phi_q \Phi_u^{-1} \quad (65)$$

Remark 5.1. The stiffness computed by employing the SBFEM is positive definite and symmetric. Hence, the stiffness matrix can be assembled in the conventional FEM approach. A simple Matlab[®] function is given in [38] to compute the stiffness matrix using the SBFEM.

Calculation of the stress intensity factors A unique feature of the SBFEM is that stress singularities, if present, are analytically represented in the radial displacement functions $\mathbf{u}(\xi)$. When a crack is modelled by a polygon with its scaling centre chosen at the crack tip in Figure (22), some of the eigenvalues $\Lambda_n^{(s)} \in \Lambda_n$ satisfy $-1 < \Lambda_n^{(s)} < 0$. These eigenvalues lead to singular stresses at the crack tip. Using $\Lambda_n^{(s)}$, the singular stress field $\sigma^{(s)}(\xi, \eta)$ can be defined as [58]

$$\sigma^{(s)}(\xi, \eta) = \Psi_\sigma^{(s)}(\eta(\theta)) \xi^{-\Lambda_n^{(s)} - \mathbf{I}_c^{(s)}} \quad (66)$$

where the singular stress mode $\Psi_\sigma^{(s)}(\eta(\theta)) = \left[\Psi_{\sigma_{xx}}^{(s)}(\eta(\theta)) \quad \Psi_{\sigma_{yy}}^{(s)}(\eta(\theta)) \quad \Psi_{\tau_{xy}}^{(s)}(\eta(\theta)) \right]^T$ is

$$\Psi_\sigma^{(s)}(\eta(\theta)) = \mathbf{D}(-\mathbf{B}_1(\eta(\theta))\Phi_u^{(s)}\Lambda_n^{(s)} + \mathbf{B}_2(\eta(\theta))\Phi_u^{(s)}) \quad (67)$$

In Equation (67) $\Phi_u^{(s)} \subset \Phi_u$ and $\mathbf{c}^{(s)} \subset \mathbf{c}$, contain the displacement modes and integration constants corresponding to $\Lambda_n^{(s)}$. It can be discerned from Equation (66) that $\Lambda_n^{(s)}$ leads to singular stresses at the crack tip. This enables the stress intensity factors to be computed directly from their definitions. The stress intensity factors for a crack that is aligned with the Cartesian coordinate axes shown in Figure (23) are defined as

$$\left\{ \begin{array}{c} K_I \\ K_{II} \end{array} \right\} = \lim_{r \rightarrow 0} \left\{ \begin{array}{c} \sqrt{2\pi r} \sigma_{yy}|_{\theta=0} \\ \sqrt{2\pi r} \tau_{xy}|_{\theta=0} \end{array} \right\} \quad (68)$$

Substituting the stress components in Equation (66) at angle $\theta = 0$ into Eq. (68) and using the

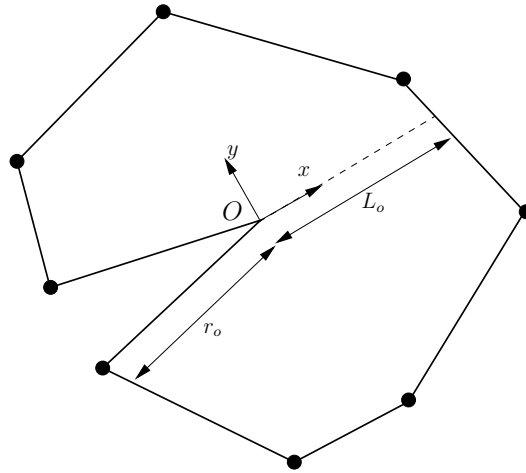


Figure 23. A cracked domain modelled by SBFEM and the definition of local coordinate system, where the ‘black’ dots represent the nodes.

relation $\xi = r/L_o$ at $\theta = 0$, the stress intensity factors are

$$\left\{ \begin{array}{c} K_I \\ K_{II} \end{array} \right\} = \sqrt{2\pi L_o} \left\{ \begin{array}{c} \Psi_{\sigma_{yy}}^{(s)}(\eta(\theta=0))\mathbf{c}^{(s)} \\ \Psi_{\tau_{xy}}^{(s)}(\eta(\theta=0))\mathbf{c}^{(s)} \end{array} \right\} \quad (69)$$

5.3.1. Plate with double edge crack in tension The plate with double edge crack subjected to a uniform tension at both ends as shown in Figure (24) is considered. In the computations, the ratio of the crack length, a , to the width of the plate, H , is $a/H = 0.25$. The material properties of the plate are: Young’s modulus, $E = 200$ GPa and Poisson’s ratio, $\nu = 0.3$. In this example, plane stress conditions are assumed. The empirical mode I SIF that is given by:

$$K_I^{\text{ref}} = C\sigma\sqrt{\pi a} \quad (70)$$

where C is a correction factor. For $a/b > 0.4$, $b = H/2$, the correction factor is given by [60]:

$$C = 1.12 + 0.203 \left(\frac{a}{b}\right) - 1.197 \left(\frac{a}{b}\right)^2 + 1.930 \left(\frac{a}{b}\right)^3 \quad (71)$$

The above correction factor is for an infinite plate with an accuracy of 2%. For the chosen parameters, the reference normalized SIF is $K_I/\sqrt{\pi a} = 1.1635$. The plate is discretized with a polygon mesh. For the polygons containing the crack tip, we employ the SBFEM technique to capture the singularity. In this polygon, each edge is further discretized with 5 linear elements so that the angular variation of the SIF can be computed accurately [39]. For the elements that does not contain the crack tip, we employ the SFEM with stabilization to compute the stiffness matrix. The convergence of the mode I SIF with mesh refinement is give in Table II. It can be seen that the proposed method converge to the empirical relation with mesh refinement.

Table II. Plate with an edge crack in remote tension: convergence of mode I SIF.

h	Number of Polygons	Number of nodes	K_I	$K_I/\sqrt{\pi a}$
0.25	32	111	1.0524	1.1875
0.125	91	247	1.0555	1.1910
0.0625	332	777	1.0452	1.1794
0.03125	1229	2659	1.0431	1.1770
0.015625	4940	10245	1.0432	1.1772

5.3.2. *Angled crack in an isotropic material* In this example, a plate with an angled crack subjected to far field bi-axial stress field, σ (see Figure (25)) with $a/w = 0.1$, $\sigma_1 = 1$ and $\sigma_2 = 2$ is considered. In this example, the mode I and the mode II SIFs, K_I and K_{II} , respectively, are obtained as a function of the crack angle β . For the loads shown, the analytical SIF for an infinite plate are given by [61]:

$$\begin{aligned} K_I &= (\sigma_2 \sin^2 \beta + \sigma_1 \cos^2 \beta) \sqrt{\pi a} \\ K_{II} &= (\sigma_2 - \sigma_1) \sin \beta \cos \beta \sqrt{\pi a} \end{aligned} \quad (72)$$

The material properties of the plate are: Young's modulus, $E = 200$ GPa and Poisson's ratio, $\nu = 0.3$. In this example, the plate is discretized with polygon meshes (containing 300 polygons). The variations of the mode I and mode II SIF with the crack orientation β are presented in Table III. It can be observed that the results from the present method agree well with the reference solutions.

Table III. Mode I and Mode II SIF for a plate with an inclined crack.

β	mode I SIF			mode II SIF		
	Equation (72)	Crack Tip A	Crack Tip B	Equation (72)	Crack Tip A	Crack Tip B
0°	1.0000	1.0176	1.0168	0.0000	0.0000	0.0000
15°	1.0670	1.0937	1.0876	0.2500	0.2343	0.2453
30°	1.2500	1.2786	1.2786	0.4330	0.4380	0.4379
45°	1.5000	1.5281	1.5266	0.5000	0.5039	0.5053
60°	1.7500	1.7893	1.7893	0.4330	0.4427	0.4429
75°	1.9330	1.9855	1.9738	0.2500	0.2880	0.2669
90°	2.0000	2.0351	2.0336	0.0000	0.0018	0.0122

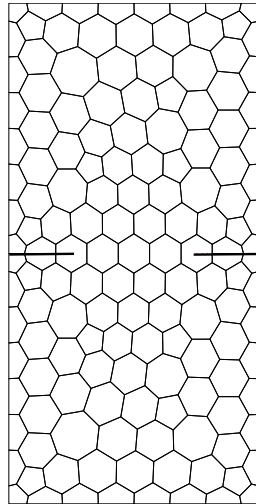
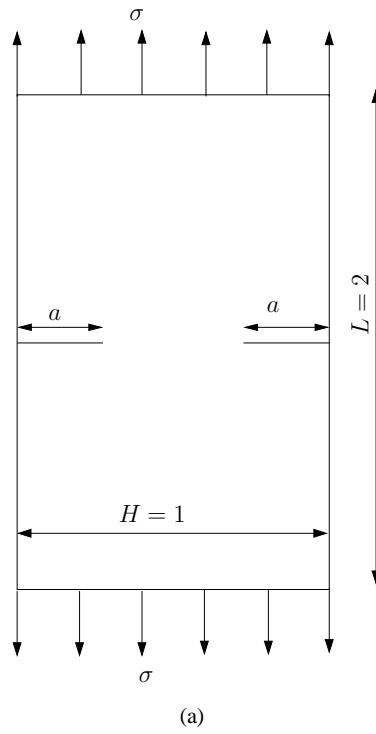


Figure 24. Plate with an edge under tension: (a) geometry and boundary conditions and (b) domain discretized with polygonal elements.

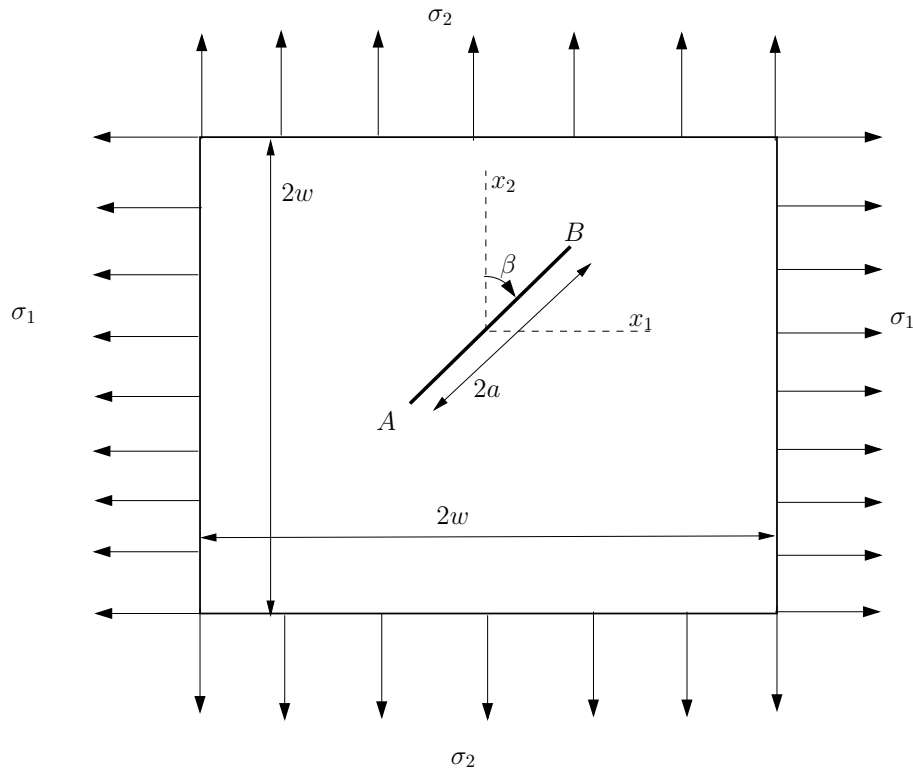


Figure 25. Plate with an oblique crack: geometry and boundary conditions.

6. CONCLUSIONS

In this paper, we revisited the cell-based SFEM and extended the method to arbitrary polygons and polyhedrons. We also demonstrated the similarity of the method with the VEM. We conclude that the SFEM is a *special case* of the more general VEM. By utilizing the concept of stabilizing term from the VEM, we have proposed a new stabilized smoothed finite element method. Instead of increasing the number of subcells, we add to the one-subcell, the stability term borrowed from the VEM. When applied to arbitrary polygons/polyhedrons, with the proposed method, sub-triangulation of the polygon/polyhedron is not required to ensure stability. From the detailed numerical study, we observe that the SFEM with stabilization term yields more accurate results than the conventional SFEM with many subcells. To study problems with singularity, the proposed method is combined with the SBFEM. The proposed method is flexible, easy to implement and yields accurate results.

ACKNOWLEDGEMENT

Sundararajan Natarajan would like to acknowledge the financial support of the School of Civil and Environmental Engineering, The University of New South Wales for his research fellowship since September 2012. The authors would also like to acknowledge Dr. Romain Quey for his generous support with the Neper software.

REFERENCES

1. Lee N, Bathe K. Effects of element distortions on the performance of iso-parametric elements. *International Journal for Numerical Methods in Engineering* 1993; **36**:3553–3576.
2. Gingold R, Monaghan J. Smoothed particle hydrodynamics: theory and application to non-spherical stars. *Mon. Not. R. Astron. Soc.* 1977; **181**:375–389.

3. Nguyen VP, Rabczuk T, Bordas S, Duflot M. Meshless Methods: A review and computer implementation aspects. *Mathematics and Computers in Simulation* 2008; **79**:763–813.
4. Melenk J, Babuška I. The partition of unity finite element method: basic theory and applications. *Computer Methods in Applied Mechanics and Engineering* 1996; **139**:289–314.
5. Belytschko T, Gracie R, Ventura G. A review of extended/generalized finite element methods for material modelling. *Modelling and Simulation in Materials Science and Engineering* 2009; **17**:043 001–1–043 001–24.
6. Peskin C. The immersed boundary method. *Acta Numerica* 2002; **11**:1–39.
7. Liu G, Nguyen T, Dai K, Lam K. Theoretical aspects of the smoothed finite element method (SFEM). *International Journal for Numerical Methods in Engineering* 2007; **71**(8):902–930.
8. Rajendran S, Ooi E, Yeo J. Mesh-distortion immunity assessment of QUAD8 elements by strong-form patch tests. *Communications in Numerical Methods in Engineering* 2007; **23**:157–168.
9. Rajendran S. A technique to develop mesh-distortion immune finite elements. *Computer Methods in Applied Mechanics and Engineering* 2010; **199**:1044–1063.
10. Sze K, Liu G, Fan H. Four- and eight-node hybrid-Trefftz quadrilateral finite element models for helmholtz problem. *Computer Methods in Applied Mechanics and Engineering* 2010; **199**:598–614.
11. Wang H, Qin QH. Fundamental-solution-based hybrid FEM for plane elasticity with special elements. *Computational Mechanics* 2011; **48**:515–528.
12. Sukumar N, Malsch E. Recent advances in the construction of polygonal finite element interpolants. *Archives of Computational Methods in Engineering* 2006; **13**(1):129–163.
13. Kagan P, Fischer A, Yoseph PZB. Mechanically based models: Adaptive refinement for B-spline finite element. *International Journal for Numerical Methods in Engineering* 2003; **57**:1145–1175.
14. Hughes T, Cottrell J, Bazilevs Y. Isogeometric analysis: CAD, finite elements, NURBS, exact geometry and mesh refinement. *Computer Methods in Applied Mechanics and Engineering* 2006; **194**:4135–4195.
15. Wrobel L, Aliabadi M. *The boundary element method*. John Wiley & Sons, New York, 2002.
16. Wolf J, Song C. The scaled boundary finite-element method - a premier derivation. *Computers & Structures* 2000; **78**:191–210.
17. Liu G, Dai K, Nguyen T. A smoothed finite element for mechanics problems. *Computational Mechanics* 2007; **39**:859–877.
18. Manzini G, Russo A, Sukumar N. New perspectives on polygonal and polyhedral finite element methods. *Mathematical Models and Methods in Applied Sciences* 2014; **24**:1665.
19. Chen J, Wang H. Some recent improvements in meshfree methods for incompressible finite elasticity boundary value problems with contact. *Computational Mechanics* 2000; **25**:137–156.
20. Liu G, Nguyen-Thoi T, Nguyen-Xuan H, Lam K. A node based smoothed finite element (NS-FEM) for upper bound solution to solid mechanics problems. *Computers and Structures* 2009; **87**:14–26.
21. Liu G, Nguyen-Thoi T, Lam K. An edge-based smoothed finite element method (ES-FEM) for static, free and forced vibration analyses of solids. *Journal of Sound and Vibration* 2009; **320**:1100–1130.
22. Nguyen-Thoi T, Liu G, Lam K, Zhang G. A face-based smoothed finite element method (FS-FEM) for 3D linear and nonlinear solid mechanics using 4-node tetrahedral elements. *International Journal for Numerical Methods in Engineering* 2009; **78**:324–353.
23. Liu G, Nguyen-Thoi T, Lam K. A novel alpha finite element method (α fem) for exact solution to mechanics problems using triangular and tetrahedral elements. *Computer Methods in Applied Mechanics and Engineering* 2008; **197**:3883–3897.
24. Nguyen-Xuan H, Bordas S, Nguyen-Dang H. Smooth finite element methods: convergence, accuracy and properties. *International Journal for Numerical Methods in Engineering* 2008; **74**:175–208.
25. Nguyen-Xuan H, Rabczuk T, Bordas S, Debongnie J. A smoothed finite element method for plate analysis. *Computer Methods in Applied Mechanics and Engineering* 2008; **197**:1184–1203.
26. Nguyen-Thanh N, Rabczuk T, Nguyen-Xuan H, Bordas SP. A smoothed finite element method for shell analysis. *Computer Methods in Applied Mechanics and Engineering* 2008; **198**:165–177.
27. Ong TH, Liu G, Nguyen-Thoi T, Nguyen-Xuan H. Inf-Suf stable bES-FEM method for nearly incompressible elasticity 2013; URL <http://arxiv.org/pdf/1305.0466.pdf>.
28. Lee CK, Mihai LA, Kerfriden P, Bordas SP. The edge-based strain smoothing method for compressible and nearly incompressible non-linear elasticity for solid mechanics 2014; URL <http://orbilu.uni.lu/bitstream/10993/14933/1/CKpaper.pdf>.
29. Bordas S, Natarajan S, Kerfriden P, Augarde C, Mahapatra D, Rabczuk T, Pont S. On the performance of strain smoothing for quadratic and enriched finite element approximations (XFEM/GFEM/PUFEM). *International Journal for Numerical Methods in Engineering* 2011; **86**:637–666.
30. Chen L, Rabczuk T, Bordas S, Liu G, Zheng K, Kerfriden P. Extended finite element method with edge-based strain smoothing (ESm-XFEM) for linear elastic crack growth. *Computer Methods in Applied Mechanics and Engineering* 2012; **209–212**:250–265.
31. Wachspress E. *A rational basis for function approximation*. Springer, New York, 1971.
32. Sukumar N, Tabarraei A. Conforming polygonal finite elements. *International Journal for Numerical Methods in Engineering* 2004; **61**:2045–2066.
33. Natarajan S, Bordas S, Mahapatra DR. Numerical integration over arbitrary polygonal domains based on Schwarz-Christoffel conformal mapping. *International Journal for Numerical Methods in Engineering* 2009; **80**:103–134.
34. Mousavi S, Xiao H, Sukumar N. Generalized Gaussian quadrature rules on arbitrary polygons. *International Journal for Numerical Methods in Engineering* 2010; **82**:99–113.
35. Talischi C, Paulino GH. Addressing Integration Error for Polygonal Finite Elements Through Polynomial Projections: A Patch Test Connection 2013; .
36. Sudhakar Y, de Almeida JM, Wall WA. An accurate, robust, and easy-to-implement method for integration over arbitrary polyhedra: Application to embedded methods. *Journal of Computational Physics* 2014; .

37. Dai K, Liu G, Nguyen T. An n -sided polygonal smoothed finite element method for solid mechanics. *Finite Elements in Analysis and Design* 2007; **43**:847–860.
38. Natarajan S, Ooi ET, Chiong I, Song C. Convergence and accuracy of displacement based finite element formulation over arbitrary polygons: Laplace interpolants, strain smoothing and scaled boundary polygon formulation. *Finite Elements in Analysis and Design* 2014; **85**:101–122.
39. Ooi ET, Song C, Tin-Loi F, Yang Z. Polygon scaled boundary finite elements for crack propagation modelling. *International Journal for Numerical Methods in Engineering* 2012; **91**:319–342.
40. da Veiga L, Manzini G. The mimetic finite difference method and the virtual element method for elliptic problems with arbitrary regularity. *Technical Report LA-UR-12-22977*, Los Alamos National Laboratory 2012.
41. da Veiga LB, Brezzi F, Cangiani A, Manzini G, Marini L, Russo A. The basic principles of virtual element methods. *Mathematical Models and Methods in Applied Sciences* 2013; **23**:199–214.
42. da Veiga LB, Brezzi F, Marini L, Russo A. The Hitchhiker's Guide to the Virtual Element Method. *Mathematical models and methods in applied sciences* 2014; **24**:1541.
43. Yoo J, Moran B, Chen J. Stabilized conforming nodal integration in the natural-element method. *International Journal for Numerical Methods in Engineering* 2004; **60**:861–890.
44. Gain AL, Talischi C, Paulino GH. On the Virtual Element Method for three-dimensional linear elasticity problems on arbitrary polyhedra meshes. *Computer Methods in Applied Mechanics and Engineering* 2014; doi:10.1016/j.cma.2014.05.005.
45. Balachandran G, Rajagopal A, Sivakumar S. Mesh free Galerkin method based on natural neighbors and conformal mapping. *Computational Mechanics* 2008; **42**:885–905.
46. Thiagarajan V, Shapiro V. Adaptively weighted numerical integration over arbitrary domains. *Computer & Mathematics with Applications* 2014; **67**:1682–1702.
47. Sommariva A, Vianello M. Gauss-Green cubature and moment computation over arbitrary geometries. *Journal of Computational and Applied Mathematics* 2009; **231**:886–896.
48. da Veiga L, Brezzi F, Cangiani A, Manzini G, Marini L, Russo A. Basic principles of virtual element methods. *Mathematical Models and Methods in Applied Sciences* 2013; **23**:199.
49. da Veiga L, Brezzi F, Marini L. Virtual elements for linear elasticity problems. *SIAM Journal of Numerical Analysis* 2013; **51**:794–812.
50. Talischi C, Paulino GH, Pereira A, Menezes IF. Polytop: a Matlab implementation of a general topology optimization framework using unstructured polygonal finite element meshes. *Struct. Multidisc Optim* 2012; **45**:329–357.
51. Quey R, Dawson P, Barbe F. Large-scale 3d random polycrystals for the finite element method: Generation, meshing and remeshing. *Computer Methods in Applied Mechanics and Engineering* 2011; **200**:1729–1745.
52. Szabó B, Babuška I. *Finite Element Analysis*. John Wiley & Sons, New York, 1991.
53. Bordas SP, Rabczuk T, Hung NX, Nguyen VP, Natarajan S, Bog T, Quan DM, Hiep NV. Strain smoothing in FEM and XFEM. *Computers & Structures* 2010; **88**:1419–1443.
54. Hung NX, Hiep NV, Bordas S, Rabczuk T, Duflot M. A cell-based smoothed finite element method for three dimensional solid structures. *KSCE Journal of Civil Engineering* 2012; **16**:1230–1242.
55. Macneal RH, Harder RL. A proposed standard set of problems to test finite element accuracy. *Finite Elements in Analysis and Design* 1985; **1**:3–20.
56. Barber J. *Elasticity*. Springer, New York, 2010.
57. Bishop J. A displacement based finite element formulation for general polyhedra using harmonic shape functions. *International Journal for Numerical Methods in Engineering* 2014; **97**:1–31.
58. Wolf J, Song C. The scaled boundary finite-element method - a fundamental solution-less boundary element method. *Computer Methods in Applied Mechanics and Engineering* 2001; **190**:5551–5568.
59. Deeks A, Wolf J. A virtual work derivation of the scaled boundary finite-element method for elastostatics. *Computational Mechanics* 2002; **28**:489–504.
60. Tada H, Paris P, Irwin G. *The stress analysis of cracks*. The American Society of Mechanical Engineers, New York, 2000.
61. Aliabadi M, Rooke D, Cartwright D. Mixed-mode Bueckner weight functions using boundary element analysis. *International Journal of Fracture* 1987; **34**:131–147.